Validation of the Aeolus L2A products with the eVe reference lidar measurements from the ASKOS/JATAC campaign

Peristera Paschou[1,2], Nikolaos Siomos[3], Eleni Marinou[1], Antonis Gkikas[4,1], Samira M. Idrissa[5], Daniel T. Quaye[6], Désiré D. Fiogbe Attannon[7], Kalliopi Artemis Voudouri[1,2], Charikleia Meleti[2], David P. Donovan[8], George Georgoussis[9], Tommaso Parrinello[10], Thorsten Fehr[11], Jonas von Bismarck[11], and Vassilis Amiridis[1]

[1]Institute for Astronomy Astrophysics Space Applications and Remote Sensing, National Observatory of Athens, Athens, Greece
[2]Laboratory of Atmospheric Physics, Physics Department, Aristotle University of Thessaloniki, Greece
[3]Meteorological Institute, Ludwig Maximilian University of Munich, Munich, Germany
[4]Academy of Athens, Athens, Greece
[5]African Youth Initiative on Climate Change-Niger (RJNCC/AYICC-Niger), Niamey, Niger
[6]Atmospheric Chemistry Department, Leibniz Institute for Tropospheric Research (TROPOS), Leipzig, Germany
[7]West African Science Service Centre on Climate Change and Adapted Land Use, Atlantic Technical University, Sao Vicente, Cabo Verde
[8]Royal Netherlands Meteorological Institute, De Bilt, The Netherlands
[9]Raymetrics S.A., Athens, Greece
[10]European Space Agency (ESA–ESRIN), Frascati, Italy
[11]European Space Agency (ESA–ESTEC), Noordwijk, The Netherlands

Correspondence to: Peristera Paschou (pepaschou@noa.gr)

Abstract.

Aeolus was an ESA Earth Explorer satellite mission launched in 2018 with a lifetime of almost five years. The mission carried the Atmospheric Laser Doppler Instrument (ALADIN), a doppler wind lidar for providing wind profiles in global scale and also vertically resolved optical properties of particles (aerosols and clouds) using the high spectral resolution lidar technique. To validate the particles' optical properties obtained from Aeolus as Level 2A products, the eVe lidar, ESA's reference system for the calibration and validation of Aeolus mission, has been deployed at the ASKOS campaign in the framework of the Joint Aeolus Tropical Atlantic Campaign (JATAC). ASKOS is the ground-based component of JATAC where ground-based remote sensing and in-situ instrumentation for aerosols, clouds, winds and radiation observations has been deployed at Cado Verde during summer 2021 and 2022 for the validation of the Aeolus products. The eVe lidar is a combined linear/circular polarization and Raman lidar specifically designed to mimic the operation of Aeolus and provide ground-based reference measurements of the optical properties for aerosols and thin clouds for the validation of the Aeolus L2A products while taking into consideration the ALADIN's limitation of misdetection of the cross-polar component of the backscattered signal. As such, in the validation study the Aeolus L2A profiles obtained from the Standard Correct Algorithm (SCA), the Maximum Likelihood Estimation (MLE), and the AEL–PRO algorithms of Baseline 16 and free from the cloud contaminated bins are compared against the corresponding cloud-free Aeolus like profiles from eVe lidar, which are harmonized to the Aeolus L2A

profiles, using the 14 collocated measurements between eVe and Aeolus during the nearest Aeolus overpass from the ASKOS site. The validation results reveal good performance for the co-polar particle backscatter coefficient being the most accurate L2A product from Aeolus with overall errors up to 2 Mm⁻¹sr⁻¹, followed by the noisier particle extinction coefficient with overall errors up to 183 Mm⁻¹, and the co-polar lidar ratio which is the noisiest L2A product with extreme error values and

40   variability. The observed discrepancies between eVe and Aeolus L2A profiles increase at lower altitudes where higher atmospheric loads, which lead to increased noise levels in the Aeolus retrievals due to enhanced laser beam attenuation, and greater atmospheric variability (e.g. PBL inhomogeneities) are typically encountered. Overall, this study underlines the strengths of the optimal estimation algorithms (MLE and AEL–PRO) with consistent performance and reduced discrepancies, while the standard inversion algorithm (SCA), which was originally developed, could be further improved particularly in the

45   retrieval of the particle extinction coefficient and lidar ratio. In addition, the SCA–Mid bin resolution profiles outperform the corresponding SCA–Rayleigh bin as expected, since Mid bin resolution is obtained when averaging the values from two consecutive SCA–Rayleigh height bins.

1 Introduction

The ESA's Earth Explorer satellite mission named Aeolus was a polar orbiting satellite that was flying from August 2018 to
50   July 2023 in a sun-synchronous dawn–dusk orbit at about 320 km altitude with a repeat cycle of 7 days[1]. Aeolus carried the first doppler wind lidar in space, the so-called ALADIN lidar (Atmospheric LAser Doppler Instrument), providing vertical profiles of the wind vector component along the instrument's Horizontal Line of sight (HLOS), at a global scale, from the ground up to ~30 km in the stratosphere (Kanitz et al., 2019; Reitebuch et al., 2020). The main goal of the Aeolus satellite mission was to improve the level of knowledge on atmospheric dynamics and numerical weather prediction (Weissmann and
55   Cardinali, 2007; Tan et al., 2007). The mission successfully fulfilled its objective to demonstrate the Doppler wind lidar technique for measuring wind profiles from space. Already, the Aeolus wind dataset have been used in applications such as demonstrating the benefits of assimilating the Aeolus wind profiles in Numerical Weather Prediction (NWP) models (e.g. Hagelin et al., 2021; Rennie et al., 2021; Rani et al., 2022; Kiriakidis et al., 2023; Martin et al., 2023), studying atmospheric circulation systems like the quasi-biennial oscillation – QBO and the El Niño–Southern Oscillation – ENSO (Ern et al., 2023;
60   Martin et al., 2023), and investigating the impact of Aeolus wind data assimilation in aerosol transport events (e.g. a volcanic ash forecast from an Etna eruption case (Amiridis et al., 2023)).

Additionally, Aeolus contributed to the monitoring of the optical properties of aerosols and thin clouds since ALADIN was also a High Spectral Resolution Lidar (HSRL) instrument (Shipley et al., 1983). ALADIN was equipped with a diode-pumped Nd:YAG laser for the emission of circularly polarized laser pulses at 355 nm in a continuous mode operation with nominal
65   pulse energy of ~80 mJ and pulse repetition rate of 50 Hz, pointing at 37.6° off-nadir (Lolli et al., 2013; Flament et al., 2021;

---

[1] The satellite Aeolus reentered from space on the 28th July 2023 but the mission continues to be funded until end 2028 with the objective to improve the products with new evolutions and better quality

Flamant et al., 2022). The backscattered signals from molecules and particles were collected with a Cassegrain type telescope of 1.5 m diameter and a FOV of 18 µrad (Reitebuch, 2012; Flamant et al., 2022) and directed to a multiple interferometer receiver unit. The multiple interferometers receiver splits the atmospheric signals into a Rayleigh channel and a Mie channel according to the difference in scattered spectra by molecules and particles attributed to the Doppler effect (Shipley et al., 1983;

70 Imaki et al., 2005; Ansmann et al., 2007). The Rayleigh channel deployed a dual Fabry-Pérot interferometer for the detection of the broadband molecular backscattered signal and the Mie channel a Fizeau interferometer for the detection of the narrowband backscatter signal from particles (Ansmann et al., 2007; Flamant et al., 2022; Flament et al., 2021). However, the separation of the pure molecular and particle contribution in the received backscattered signal in the Rayleigh and the Mie channels, respectively, is not ideal due to the transmission curves of the interferometers leading to a cross-talk effect in both

75 channels (Flament et al., 2021; Flamant et al., 2022).

The Rayleigh channel is used for the retrieval of the particle extinction coefficient and the combination of the Rayleigh and Mie channels for the retrieval of the particle backscatter coefficient; the lidar ratio is calculated from the ratio of the two products (extinction-to-backscatter ratio). The particle extinction and backscatter coefficients, the lidar ratio as well as scattering ratio and the aerosol optical depth (AOD) constitute the Level 2A (L2A) spin-off products. However, the

80 transmit/receive design of ALADIN allows the detection of only the co-polar component of the collected backscattered signal (ESA, 2008; Flamant et al., 2022) which affects the retrieval of the particle backscatter coefficient resulting to the derivation of a parameter that can be called as co-polar particle backscatter coefficient (Appendix A; Paschou et al., 2022). In cases where depolarizing particles are present in the measured atmospheric scene, the co-polar particle backscatter coefficient obtained from Aeolus is highly underestimated compared to the total particle backscatter coefficient that is measured from the typical

85 depolarization lidars detecting both the co- and the cross-polar components of the backscattered lidar signal. Similarly, under the presence of depolarizing particles the co-polar lidar ratio from Aeolus is overestimated compared to the total lidar ratio. The particle extinction coefficient is not affected by this limitation arising from the ALADIN design since it is retrieved using only the molecular backscattered lidar signals (Rayleigh channel) (Flament et al., 2021; Flamant et al., 2022).

The spectrometers in the Rayleigh and Mie channels record the analyzed lidar signals by accumulating the signal received

90 from 20 consecutive laser pulses. The recorded signal from the accumulation of 20 laser pulses is called measurement and corresponds to Aeolus' finest resolution of 3 km horizontal distance. The optical products are retrieved using an averaging of 30 consecutive measurements per profile in the observation level (also called Basic Repeat Cycle; BRC) resulting to a resolution of ~87 km horizontal distance. Moreover, the lidar signals are detected in both channels with a ranging resolution of 24 vertical bins. The resolution of each vertical bin varies from 0.25 to 2 km (always a multiple of 0.25 km). The altitude

95 limits (lower and upper) and the thickness of each bin can be adjusted, separately for each channel, through the Range Bin Settings (RBS) that are applied depending on the sampling strategy and the reduction of the signal noise levels. For example, thin bins with thickness of e.g. 0.25 km are preferred close to the surface where the variability of the aerosols and the wind components is expected to be higher (Flament et al., 2021; Flamant et al., 2022).

Like every satellite mission with a lidar onboard, e.g. CALIPSO (Winker et al., 2010) and CATS (Yorks et al., 2014), Aeolus
100 has to undergo through validation of its products for the evaluation of its overall performance and the identification of possible
observation biases, induced by the lidar design and its limitations and/or the retrieval algorithms, that could affect the quality
of the products. For the Aeolus wind product, a plethora of validation studies have been performed using ground-based and
airborne wind lidar measurements (Witschas et al., 2020; Lux et al., 2022; Witschas et al., 2022; Abril-Gago et al., 2023),
radiosondes (Baars et al., 2020; Ratynski et al., 2023; Borne et al., 2024), and NWP model equivalent data (Martin et al., 2021;
105 Liu et al., 2022; Zuo et al., 2022). The outcome of these Cal/Val studies revealed a very good performance of the wind products,
as a result of upgrades in the wind retrieval algorithm with corrections and calibration improvements. More specifically, the
systematic errors for both products (Rayleigh and Mie winds) and the random error for Mie winds fall within the mission
requirements and the ESA recommendations (i.e. systematic errors up to 0.7 ms^{-1} and random errors up to 2.9 ms^{-1} for both
products) while random errors up to 4.8 ms^{-1} are found for Rayleigh winds in Borne et al., (2024).

110 On the contrary, for the L2A aerosol products, a limited number of studies were performed focusing mainly on the validation
of the L2A particle backscatter coefficient obtained from the Standard Correct Algorithm (SCA). More specifically, Baars et
al., (2021) reported very good agreement between the Aeolus L2A particle backscatter coefficient (i.e. the Aeolus co-polar
particle backscatter coefficient) and the ground-based Aeolus like particle backscatter coefficient and good agreement for the
particle extinction coefficient. The validation study performed using as reference a PollyXT lidar operating in Leipzig during
115 a Californian wildfire smoke transport event over Europe. However, the observed larger differences between Aeolus and the
ground-based profiles inside the Planetary Boundary Layer (PBL) were attributed to the Aeolus coarser horizontal resolution
and to the spatiotemporal inhomogeneous conditions of the boundary layer. In addition, a statistical validation study was
performed by Abril-Gago et al., (2022) on the Aeolus L2A particle backscatter coefficient using the SCA algorithm (Baseline
10) for the Aeolus profiles and ground-based lidar observations under cloud-free conditions at three ==ACTRIS/EARLINET==
120 lidar stations in the Iberian Peninsula; a region mainly affected by dust and continental/anthropogenic aerosols. The statistical
analysis applied for each lidar station with the maximum values among the different stations to be a mean bias of -0.16 ± 0.04
Mm^{-1}sr^{-1} with RMSE of 0.6 ± 0.2 Mm^{-1}sr^{-1} for the SCA–Rayleigh bin profiles (Granada) and a mean bias of 0.11 ± 0.08 Mm^{-1}sr^{-1} with RMSE of 0.25 ± 0.11 Mm^{-1}sr^{-1} for the SCA–Mid bin (Evora). Gkikas et al., (2023) performed a statistical validation
study of the Aeolus L2A particle backscatter coefficient using ground-based lidar observations from three lidar stations in the
125 Eastern Mediterranean contributing to the Greek national research infrastructure PANACEA, which is an ACTRIS component.
The location of lidar stations in the eastern Mediterranean allowed the validation of the Aeolus L2A aerosol products from the
SCA algorithm (Baseline 11) under different aerosol species originating from natural (e.g. marine, dust, biogenic, and volcanic
particles) or anthropogenic sources. The comparison between the Aeolus L2A particle backscatter coefficient and the ground-
based total particle backscatter coefficient for cloud free collocated measurements (removal of cloud contaminated cases using
130 auxiliary MSG-SEVIRI data) from all stations revealed better agreement between Aeolus and the ground-based profiles with
respect to the comparison for the total number of collocated measurements (i.e. without removing the cloud contaminated
cases). The overall absolute bias has been reduced from 0.45 to 0.27 Mm^{-1}sr^{-1} and from 0.69 to 0.37 Mm^{-1}sr^{-1} for the Aeolus

SCA–Rayleigh bin profiles and SCA–Mid bin profiles, respectively, and the overall RMSE has been reduced from 2 to 1.65 Mm⁻¹sr⁻¹ and from 1.88 to 1 Mm⁻¹sr⁻¹ for the Aeolus SCA–Rayleigh and SCA–Mid bin profiles, respectively. Additionally, the

135   vertically resolved statistical analysis by Gkikas et al., (2023) showed that the performance of the SCA retrievals is decreased at the lowermost bins probably due to the contamination from surface return signals or the increased SNR levels close to the surface, which is in line with the findings of Abril-Gago et al., (2022). Finally, all three studies (Baars et al., 2021; Abril-Gago et al., 2022; Gkikas et al., 2023) conclude that the SCA–Mid bin profiles demonstrate better agreement with the ground-based reference profiles compared to the SCA–Rayleigh bin due to the averaging of two neighbouring height bins. However, the

140   above studies lack of comparisons for the Aeolus L2A extinction coefficient and lidar ratio profiles as well as the evaluation of the Aeolus L2A profiles from the rest Aeolus algorithms (e.g. the MLE and the AEL–PRO which, however, they only became available in later versions of the L2A processors).

In this study, we use the eVe lidar, the ESA's reference lidar, designed specifically to mimic the operation of ALADIN and provide reference measurements of the aerosol optical properties for the validation of the corresponding Aeolus L2A products

145   (backscatter coefficient, extinction coefficient, and lidar ratio) as obtained from the SCA, the MLE, and the AEL–PRO L2A processors using the latest algorithms' version (Baseline 16). More specifically, we use a dataset of collocated eVe lidar measurements with Aeolus overpasses during the ASKOS/JATAC experimental campaign that was held in summer of 2021 and 2022 at the Cabo Verde islands.

2 Methods and datasets

150   **2.1 The ASKOS/JATAC campaign**

A dedicated large-scale experimental campaign with the participation of groups from both EU and NASA has been organized by ESA to support the validation of Aeolus and the preparation of the ESA missions EarthCARE (Illingworth et al., 2015; Wehr et al., 2023) and WIVERN. The so-called Joint Aeolus Tropical Atlantic Campaign (JATAC) included both ground-based and airborne deployments on Cabo Verde (2021/2022) and the US Virgin Islands (2021). The joint activities resulted in

155   high-quality and comprehensive dataset of aerosol, clouds and wind measurements from multiple in-situ and remote sensing instruments to support: i) the validation of Aeolus and other satellites as well as the development of future EO missions and ii) a wide range of scientific objectives related to the Saharan Aerosol Layer, Inter-Tropical Convergence Zone, and tropical jet streams and their impact on convective systems, long range dust transport events and air quality (Fehr et al., 2023). The ground-based component of JATAC, named ASKOS, was held at the Ocean Science Centre of Mindelo (OSCM) on the island

160   of São Vicente in Cabo Verde and implemented in three intense phases (September 2021, June 2022, September 2022) (Marinou et al., 2023). The Cabo Verde environment is ideal for aerosol studies and desert dust specifically. Situated downwind of the Sahara Desert, Cabo Verde receives a large influx of dust, particularly in summer during the peak of the dust season (Gkikas et al., 2021), thus constituting a suitable location for the evaluation of the Aeolus performance under dust-rich environments.

165   For the ASKOS operations, a remote sensing facility for wind, aerosols, and clouds was set up comprising of aerosol and wind lidars, a sun-photometer, a cloud radar, and a radiometer. One of the ASKOS lidars was the ESA's eVe reference lidar that was deployed to provide reference measurements of the optical properties of aerosols and thin clouds serving as ground-truth for the Aeolus L2A products. Next to these remote sensing facilities, additional instrumentation has been deployed for providing measurements on particle orientation and characterization, meteorological parameters, atmospheric electricity, and

170   solar radiation. More details about the full ASKOS instrumentation is provided in Marinou et al., (2023). Moreover, according to Marinou et al., (2023), the aerosol conditions above Mindelo São Vicente during the ASKOS period as observed from the deployed instrumentation included particles within the marine boundary layer at altitudes up to 1 km and a Saharan Air Layer (SAL) extending up to 6 km. The macrophysical characteristics of the SAL (e.g. base height, depth) and the amount of desert dust particles fluctuated throughout the campaign, comprising an environment with a wide range of aerosol conditions. More

175   than nine dust transport events have been observed during ASKOS (preparatory and intense phases) usually comprising of pure SAL layers, while two of them formed a layer with desert dust and pollution mixture and a layer with desert dust and volcanic aerosols mixture. The volcanic aerosols, originated from the Cumbre Vieja volcano (19 September 2021;Córdoba-Jabonero et al., 2023) at La Palma Island, Canary Islands, were observed within the marine boundary layer, where it was mixed with marine aerosols, and at the SAL where it was mixed with dust particles (Gebauer et al., 2024).

2.2 The eVe lidar

The eVe lidar is a combined linear/circular polarization lidar system with Raman capabilities designed to be the ESA's ground reference system for the calibration and validation of the aerosol products from the ESA Aeolus satellite mission. A detailed description about the system design and specifications can be found in Paschou et al., (2022). The lidar configuration consists of two emission units with Nd-YAG lasers with pulse energies of 89 and 100 mJ at 355 nm and a repetition rate of 20 Hz, and

185   two detection units under the two Cassegrain type telescopes of 200 mm aperture and Field-Of-View (FOV) of 2.4 mm for recording the optically separated backscatter signals, in terms of polarization state and elastic/inelastic backscattering, into five PhotoMultiplier Tubes (PMTs). This dual-laser/dual-telescope configuration enables the simultaneous emission of linearly and circularly polarized light pulses at 355 nm and the detection of the elastically backscattered light with polarization sensitive channels as well as the inelastic (Raman) backscattered light at 387 nm. Each detection unit (one for linear and one for circular

190   polarization) uses two polarization sensitive channels, one for detecting the cross component of the backscattered polarized light and one for detecting the parallel component of the backscattered polarized light. In addition, a Raman channel is equipped and placed in one of the detection units, enabling the detection of the inelastic backscattering from both linearly and circularly polarized emission since each telescope receives return signals from both lasers. Hence, eVe derives vertical profiles of the aerosol backscatter coefficient, the aerosol extinction coefficient (nighttime product), the lidar ratio (nighttime product), the

195   volume and particle linear depolarization ratios, and the volume and particle circular depolarization ratios at 355 nm. Moreover, the system allows the adjustment of the measurement zenith and azimuth angle which along with its dual-laser/dual-telescope

configuration constitute the lidar capable of reproducing the operation and the pointing geometry of any ground- or space-based lidar that uses linearly or circularly polarized emission.

The eVe lidar ~~deployed on the ASKOS/JATAC campaign and~~ performed lidar measurements during the whole ASKOS period

200 including also the preparatory phase of ASKOS in July 2021. The acquired eVe dataset during ASKOS includes testing and routine measurements at multiple pointing angles (vertical and off-zenith) during daytime and nighttime as well as measurements implementing the dual-FOV technique (Paschou et al., 2023). In the current study we are using the routine linear/circular depolarization measurements that were performed during the nearest Aeolus overpass from the OSCM/ASKOS site every Friday evening (the distance of the nearest BRC from the ASKOS location spans from 9 to 48 km), when eVe was

205 pointing at 37.6° off-zenith towards Aeolus track in order to reproduce the Aeolus measurements from the ground. In total, 14 collocated eVe – Aeolus measurements were collected under multiple aerosol conditions such as pure dust, marine and dust mixtures, and volcanic mixtures with marine and dust aerosols (Marinou et al., 2023) for the validation of the Aeolus L2A products. The collocation criteria comprise a spatial collocation of maximum distance between the Aeolus overpass and the ASKOS location of 100 km and a temporal window of ±1.5 hr from the Aeolus overpass time.

210 For these 14 linear/circular depolarization measurements from eVe lidar and additionally to the routine eVe products mentioned above (i.e. particle extinction and backscatter coefficients, lidar ratio, and depolarization ratios), the profiles of the Aeolus like particle backscatter coefficient and lidar ratio were retrieved. The Aeolus like profiles are the ground-based lidar products harmonized with the Aeolus Level 2A products while considering the misdetection of the cross-polar component of the backscattered light from Aeolus (Appendix A; Paschou et al., 2022). As such, in the following results for the comparison

215 of the eVe profiles with the corresponding Aeolus L2A profiles, the eVe profiles of the particle extinction coefficient, the Aeolus like particle backscatter coefficient, and the Aeolus like lidar ratio were used as the reference.

2.3 The Aeolus Level 2A processors

During the development phase of Aeolus, two independent processors have been developed, one for the retrieval of the wind profiles as L2B products (Tan et al., 2008), and one for the retrieval of the optical properties of aerosols and thin clouds as

220 L2A products (Flamant et al., 2008; Flament et al., 2021). In general, the L2A processor uses as input (Rennie et al., 2020; Flamant et al., 2022): i) the pre-processed signals from the Mie and Rayleigh channels corrected from noise sources and instrumental effects (i.e., the L1B profiles), ii) auxiliary meteorological profiles such as temperature, pressure, humidity, etc., provided from the European Centre for Medium Range Weather Forecasts – ECMWF, and iii) auxiliary calibration coefficients about the radiometric efficiency of the receiver.

225 In the beginning, the L2A processor included the historical algorithms for the Aeolus L2A products, namely the Standard and the Mie Correct Algorithms (SCA and MCA; Flamant et al., 2008; Flament et al., 2021). After launch, the L2A processors have undergone updates and improvements under releases of newer versions (i.e. Baselines) and, also, new algorithms have been added in the L2A processors such as the AEL–PRO in Baseline 12, which is an adaptation of the ATLID/EarthCARE retrieval algorithm for aerosol properties to Aeolus (Donovan et al., 2024a; Wang et al., 2024), and the Maximum Likelihood

230   Estimation (MLE; Ehlers et al., 2022) in Baseline 14. In this validation study, the Aeolus L2A profiles are obtained from the SCA, the MLE and the AEL–PRO algorithms from Baseline 16 of the L2A processor. A brief description on the main principles of each algorithm is provided in the following subsections.

2.3.1 Standard Correct Algorithm – SCA

The Standard Correct Algorithm (SCA) along with the Mie Correct Algorithm (MCA) have been developed by the Institute
235   Pierre Simon Laplace (IPSL) and Météo-France. The SCA algorithm uses both the measured signals from the Rayleigh and the Mie channel for the retrieval of the optical properties (co-polar particle backscatter and extinction coefficients, co-polar lidar ratio). On the other hand, the MCA is designed to use the Mie channel only as a backup solution when the SCA fails to provide retrievals (e.g. Rayleigh signals unavailable or Rayleigh and Mie height bins fail to match). The main drawback of the MCA is the use of a pre-fixed lidar ratio value of 14.3 sr for the derivation of the particle backscatter and extinction coefficients.
240   A detailed description for SCA and MCA is provided in the Algorithm Theoretical Basis Document for the Aeolus L2A products (Flamant et al., 2022) and in (Flament et al., 2021). In this study we use only the SCA profiles, thus the following discussion is focused on the SCA principles.

Briefly, the measured signals from the Rayleigh (S_{ray}) and Mie (S_{mie}) channels are a function of the instrument calibration constants (e.g. radiometric calibration coefficients K_{ray} and K_{mie}, pulse energy, number of accumulated pulses for a BRC),
245   the cross-talk coefficients $C_{i=1,2,3,4}$, the lidar range R, the pure molecular and particle backscattering contributions to the signals (X and Y), and the atmospheric transmission from the lidar to the target and back (Eqs. 1 – 6 ; Flament et al., 2021). The measured signals are corrected from the cross-talk effect and the pure molecular (X) and particle (Y) signals are obtained. Then, the Aeolus particle backscatter coefficient is obtained from the ratio $\frac{Y}{X}$ multiplied with the molecular backscatter coefficient as calculated from the auxiliary meteorological data (Eqs. 9 and 10; Flament et al., 2021). The particle extinction
250   coefficient is retrieved using the molecular signal X in an iterative process from the top of the profile to the bottom taking into account the attenuation from the overlying height bins while assuming that the particle extinction in the topmost bin (i.e. first bin) is zero (Eqs. 11 – 14; Normalized Integrated Two-Way Transmission method; Flament et al., 2021) and uniform particle layers fill the entire range of each bin. However, the normalization of the molecular signal in the first bin makes the retrieval of the extinction coefficient susceptible to the noise of the fist bin (usually between 20 – 25 km) where the molecular signal is
255   the lowest compared to the rest height bins. As such, the differentiation of two consecutive bins can lead to unrealistic high extinction values (positive or negative) due to the level of attenuation in the simulated molecular signals (Flament et al., 2021). To mitigate the propagation of the large error of the first bin to the underlying bins due to the negative extinction values (Flament et al., 2021; Flamant et al., 2022) and create a more reliable and less biased extinction retrieval, a new particle extinction profile is created after averaging the extinction values (including negative values) of two consecutive height bins,
260   called as SCA–Mid bin particle extinction. The averaging of values from two consecutive height bins is also applied in the retrieved backscatter profile in order to obtain the SCA–Mid bin particle backscatter coefficient and lidar ratio. As such, the

optical properties from SCA are provided in BRC level with two different vertical resolution scales: i) 24 vertical bins of the Rayleigh channel (SCA–Rayleigh bin) and ii) 23 vertical bins (SCA–Mid bin) after averaging the values of two consecutive bins.

2.3.2 Maximum Likelihood Estimation – MLE

The Maximum Likelihood Estimation method has been developed aiming to improve the Aeolus L2A retrievals by taking into account the different noise levels in the Rayleigh and Mie channels, the coupled retrieval of the backscatter and extinction coefficients, and the physical constrains on the values of the retrieved optical properties. A detailed description on the MLE approach is provided in Ehlers et al., (2022) and in the Algorithm Theoretical Basis Document for the Aeolus L2A products (Flamant et al., 2022).

In brief, the MLE concept uses an optimal estimation retrieval method with a forward model $y = F(x)$ that maps the optical properties of co-polar particle backscatter coefficient and lidar ratio (state vector x) onto the signals S_{ray} and S_{mie} (measurement vector y) (Eq. 11; Ehlers et al., 2022). The retrieval problem is a nonlinear regression problem and to obtain an accepted physical solution of the true optical properties, a minimization of a cost function (Eqs 13 – 15; Ehlers et al., 2022) is required, which describes the deviations between the measured signals (measurement state) and the forward-modelled signals. The minimization of the cost function is performed using a Limited-Memory Broyden–Fletcher–Goldfarb–Shanno algorithm with box constraints (L–BFGS–B). The applied constraints include the lidar ratio values ranging from 2 to 200 sr and positive values of backscatter and extinction coefficients. Moreover, the initialization of the cost function (i.e. the first guess) consists of an aerosol-free atmosphere with zero optical depth and a co-polar lidar ratio of 60 sr. According to Ehlers et al., (2022), the MLE retrievals may suffer from noise amplification, thus an iterative approach is followed where the cost function minimization problem is being solved iteratively until the average cost function value per bin reaches values below 1. Finally, the MLE retrievals are provided in BRC level with a vertical resolution of 24 bins similar to SCA–Rayleigh bin.

2.3.3 ATLID Aerosol Profile Algorithm for Aeolus – AEL–PRO

The AEL–PRO algorithm consists an adaptation of the aerosol profile retrieval algorithm (A–PRO) that has been developed in the Royal Netherlands Meteorological Institute (KNMI) for ATLID lidar onboard the EarthCARE satellite mission and is part of the EarthCARE L2 processors for the retrieval of the aerosol optical properties profiles using the ATLID lidar signals (Donovan et al., 2024b). In the same context, the ATLID Feature Mask (A–FM; van Zadelhoff et al., 2023) algorithm developed to provide a probability mask for the presence of atmospheric features in the ATLID lidar profiles (e.g. clear conditions, clouds, aerosols) has been adapted to Aeolus measuring principles named as AEL–FM. The main differences between A–PRO/A–FM and AEL–PRO/AEL–FM lay in the detection of only the co-polar component of backscattered signal, the adjustable range bin settings and the coarser and variable size of the height bins, the large along-track pixel size, and the large viewing angle of 37.6º off-nadir in the Aeolus measurements (Wang et al., 2024). A detailed description on the AEL–

PRO algorithm is provided in the corresponding Aeolus L2A Algorithm Theoretical Basis Document for AEL–FM and AEL–PRO (Donovan et al., 2024a) and in Wang et al., (2024).

295 In contrast to SCA and MLE algorithms using the signals from both Rayleigh and Mie channels, the AEL–PRO algorithm uses only the Mie channel for the separation of the measured signal into the cross-talk corrected "pure" molecular (Rayleigh) and particle (Mie) attenuated backscatter profiles (Fig. 2; Donovan et al., 2024a). More specifically, the measured Mie signal is derived from the detector's central region pixels where the Mie response is located, whereas the Rayleigh signal is derived from the pixels in the wing areas of the Mie response (Fig. 1; Wang et al., 2024). The cross-talk effect in the measured Rayleigh

300 and Mie signals still exists, thus the signals have to be cross-talk corrected before being used (as pure Rayleigh and Mie signals) in the retrieval of the optical properties. The advantages of this approach are i) the degrees of freedom in the system are reduced since only the calibration parameters related to the Mie channel have to be taken into account (i.e. cross-talk coefficients $C_{i=3,4}$ and radiometric calibration coefficient K_{mie}) allowing the constrain of the error magnification in lower levels, and ii) the thickness and height range of each bin are common for both signals since the signals are derived solely from the Mie channel.

305 The algorithm follows a multiscale, forward modelling optimal estimation approach which is implemented in two passes (Fig. 3; Wang et al., 2024) and the cost function is minimized using the BFGS procedure (Donovan et al., 2024a). The measurement vector $\boldsymbol{y}$ includes the cross-talk corrected pure Rayleigh and Mie attenuated backscatter signals and the state vector $\boldsymbol{x}$ includes the log base 10 form of the particle extinction coefficient, the co-polar lidar ratio, the particle effective radius, and a factor for calibration errors. The log form is used as a positivity constrain for the state vector's elements. Here, the cost function is

310 composed by the sum of two terms, one describing the deviations between the measurement state and the forward-modelled measurements and one describing the deviations between the state and an a-priori state (Eqs. 1 – 5; Wang et al., 2024). The two-pass approach is used to process both strong (i.e. clouds) and weak (i.e. aerosols) features. In the first pass, the algorithm separates the strong and weak features using the pure Mie and Rayleigh signals, the auxiliary meteorological profiles and the AEL–FM outputs and solves the optimal estimation problem for the weak features in a BRC level (horizontal resolution of

315 about 90 km). The retrievals of weak features from the first pass are then used as an a-priori state for every measurement in the second pass where the optimal estimation problem is being solved again to obtain the final L2A products (including strong features/cloudy regions) at measurement level (horizontal resolution of about 3 km) with vertical resolution of 24 bins of the Mie channel.

3. Results

320 The validation results include one case study for the one-by-one comparison between the eVe L2 and the Aeolus L2A profiles and the outcome of the statistical analysis that has been performed on the eVe – Aeolus comparison using all the 14 collocated measurements. The collocation between eVe and Aeolus is performed by selecting the nearest Aeolus BRC from the ASKOS site falling within a radius of 100 km from the site (Fig. 1) within a temporal window of ±1.5 hr from the overpass time. The distance of the nearest BRC from the ASKOS site spans from 9 to 48 km for the 14 available overpasses during ASKOS.
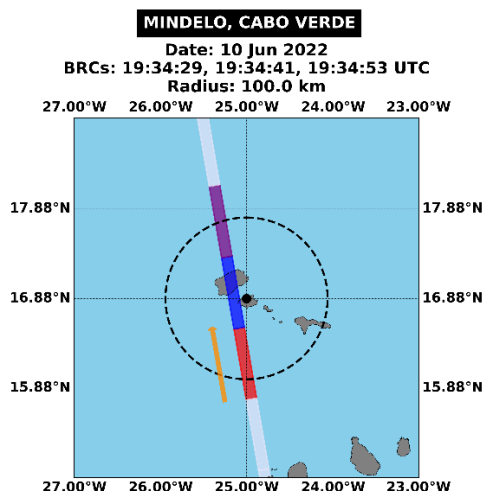
325 **Figure 1: Example of selection of the nearest Aeolus overpass (blue rectangle) from the ASKOS site on 10 June 2022. The white stripe indicates the Aeolus measurement track, the orange arrow denotes the Aeolus flight direction (ascending orbit), and the coloured rectangles correspond to the maximum three Aeolus observations (BRCs) that can be recorded falling within a radius of 100 km (dashed black line) of the ASKOS location (Mindelo, Cabo Verde; black dot). The BRC timeframes are given in the plot's title.**

330 In both one-by-one comparison case and statistical analysis, the averaged eVe L2 profiles are obtained from lidar signals from cloud-free timeframes favoring nighttime conditions for the availability of the particle extinction coefficient and lidar ratio retrievals. In the same context, the cloud flag provided per bin and in BRC level from the SCA algorithm has been applied to all available Aeolus L2A profiles from SCA, MLE, and AEL–PRO algorithms aiming for cloud-free Aeolus profiles using a common cloud masking approach. On the other hand, the Aeolus quality assurance flags are not taken into account in the

335 current study, since the application of further flagging results in significant reduction of the available bins per profile per BRC for the comparisons.

3.1 A pure dust case study

On 10th September 2021 Aeolus overpassed ~24 km westwards from Mindelo, Cabo Verde around 19:37 UTC while eVe lidar was measuring from the ground. For the comparison with the corresponding Aeolus L2A profiles, the eVe L2 profiles have

340 been retrieved inside a cloud-free time window (20:41 to 21:09 UTC) of the nighttime measurement, approximately 1 hour after the overpass, aiming to obtain not only the particle backscatter coefficient but also the particle extinction coefficient and lidar ratio profiles using the Raman inversion method. According to Fig. 2, the aerosol conditions above Mindelo during the Aeolus overpass on 10 September 2021 indicate presence of marine aerosols inside the planetary boundary layer (PBL) which are topped with a pure desert dust layer up to 6 km. The marine aerosols layer, which extending up to 1 km, has a lidar ratio

345 of 18 sr and PLDR of 0.03 while the pure dust layer that reaches up to 6 km, has lidar ratio of 50 sr and PLDR of 0.27.
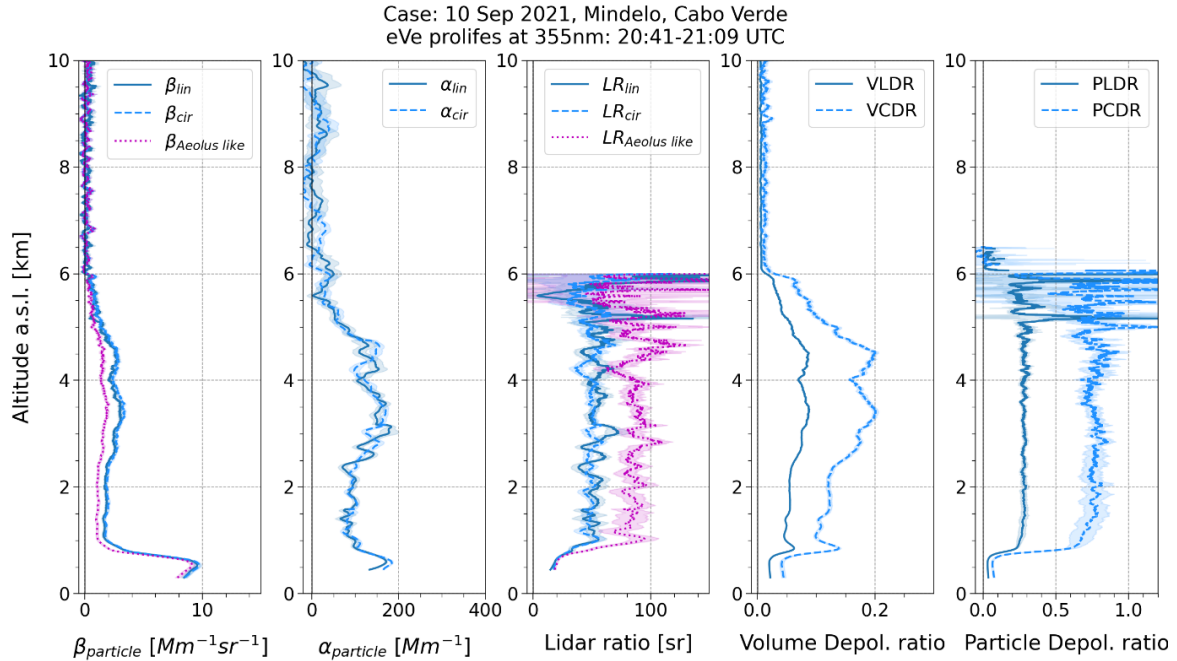
Figure 2: Averaged and cloud-free eVe L2 profiles of particle backscatter (βparticle) and extinction (αparticle) coefficients, lidar ratio, volume linear/circular depolarization ratios (VLDR/VCDR), and particle linear/circular depolarization ratios (PLDR/PCDR) at 355 nm from linear (solid; dark blue) and circular (dashed; blue) emission, during the Aeolus overpass on 10 September 2021. The Aeolus like profiles (dotted; purple) of backscatter coefficient and lidar ratio have been calculated using the circular polarization
350 **profiles.**

The eVe L2 profiles of the Aeolus like particle backscatter coefficient, the particle extinction coefficient, and the Aeolus like lidar ratio are used in the one-by-one comparison of the corresponding cloud masked Aeolus L2A products from the SCA algorithm (Fig. 3) and the MLE and AEL–PRO optimal estimators (Fig. 4). It has to be noted that the applied cloud flagging from SCA algorithm results in the comparison between eVe and Aeolus L2A in heights above 2 km where the dust layer resides (1.5 to 6 km; Fig. 2), since in lower heights the Aeolus bins are flagged as cloud contaminated from the SCA cloud

355 flag product and have been excluded from the comparisons.

For the comparison in the particle (co-polar) backscatter coefficient, the Aeolus profile from all three algorithms is in good agreement with the Aeolus like backscatter coefficient from eVe within the altitude range spanning from 2.5 to 5.5 km. The SCA–Mid bin backscatter demonstrates better performance compared to the SCA–Rayleigh bin since the maximum bias (bias

360 = Aeolus - eVe) found for the SCA–Mid is 0.56 Mm^{-1}sr^{-1} while for the SCA–Rayleigh bin is 1.2 Mm^{-1}sr^{-1} in absolute values (Fig. 3; left plot). However, the Aeolus backscatter values from SCA in the height bin at ~2 km are below zero resulting to increased bias of -0.59 Mm^{-1}sr^{-1} for the SCA–Mid bin and -1.53 Mm^{-1}sr^{-1} for the SCA–Rayleigh bin. For the optimal estimators, the maximum bias found for AEL–PRO in 0.6 Mm^{-1}sr^{-1} and for MLE is 0.41 Mm^{-1}sr^{-1} (Fig. 4; left plot). For the comparison of the particle extinction coefficient inside the dust layer, larger deviations are found between the SCA Aeolus and eVe profile

365 where the absolute biases reach up to 272.8 Mm^{-1} for SCA–Rayleigh bin and 124.2 Mm^{-1} for SCA–Mid bin (Fig. 3; middle

plot). The comparison is improved when the optimal estimators are used against eVe, with the absolute biases for MLE and AEL–PRO profiles varying from 13.1 to 98.9 Mm^{-1} and from 23.6 to 55.2 Mm^{-1}, respectively (Fig. 4; middle plot). Finally, for the comparison of the (co-polar) lidar ratio, the Aeolus profiles are considerably noisier than the corresponding Aeolus like lidar ratio from eVe. The absolute bias values for the SCA profiles inside the dust layer are considerably high since they range

370   from 30 to 127 sr, thus no good agreement can be observed between Aeolus and the eVe Aeolus like profile (Fig. 3; right plot). For the AEL–PRO and the MLE profiles the departures from the eVe Aeolus like profile are smaller than those for the SCA profiles and a good agreement can be noted only at certain height bins, at ~3 and ~4.5 km for AEL–PRO with a bias of 11 sr and at ~3.7 km for MLE with a bias of 4 sr (Fig. 4; right plot).
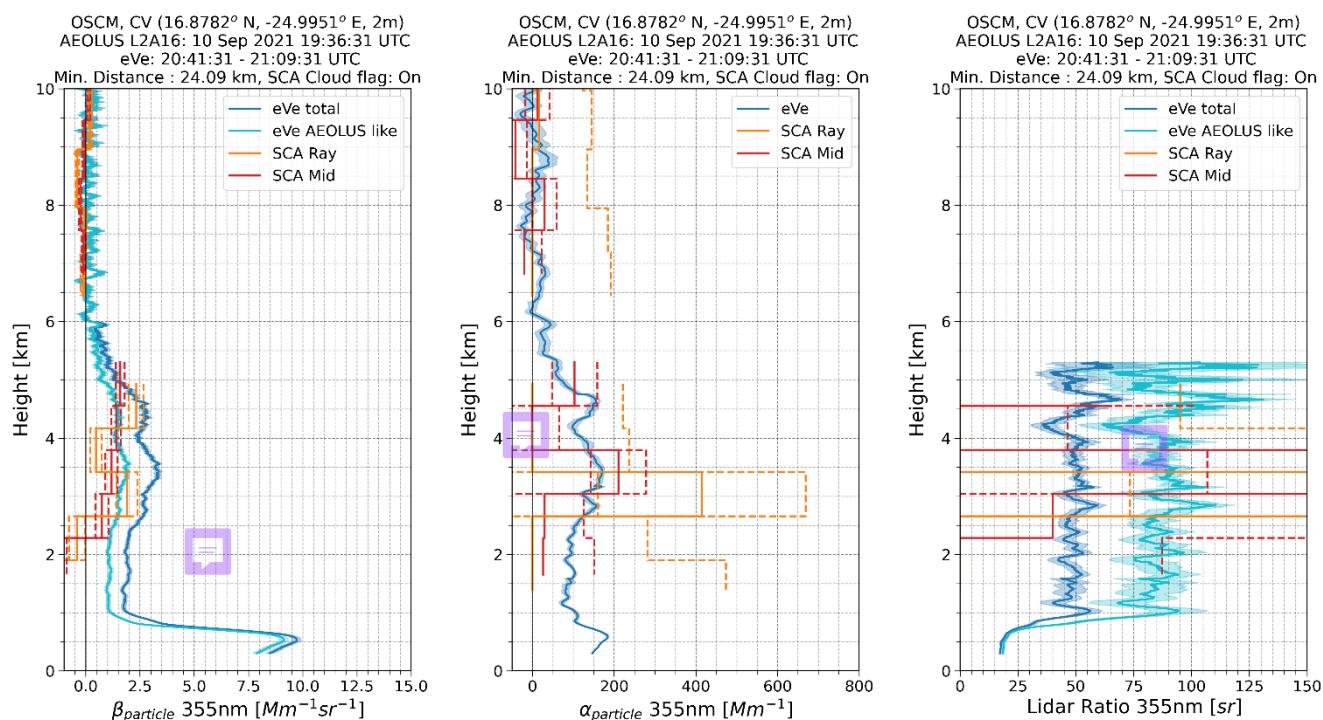
Figure 3: Comparison of the cloud masked SCA Aeolus L2A profiles (SCA–Rayleigh bin in orange; SCA–Mid bin in red) from
375   **Baseline 16 against eVe L2 lidar products for the Aeolus overpass on 10 September 2021. The averaged eVe lidar profiles of the Aeolus like particle backscatter (Aeolus like $\beta_{particle}$), particle extinction coefficient ($\alpha_{particle}$), and Aeolus like lidar ratio were retrieved within the timeframe 20:41 to 21:09 UTC. The uncertainty of retrievals is denoted with shaded regions in the eVe profiles and with dashed lines in the Aeolus profiles.**
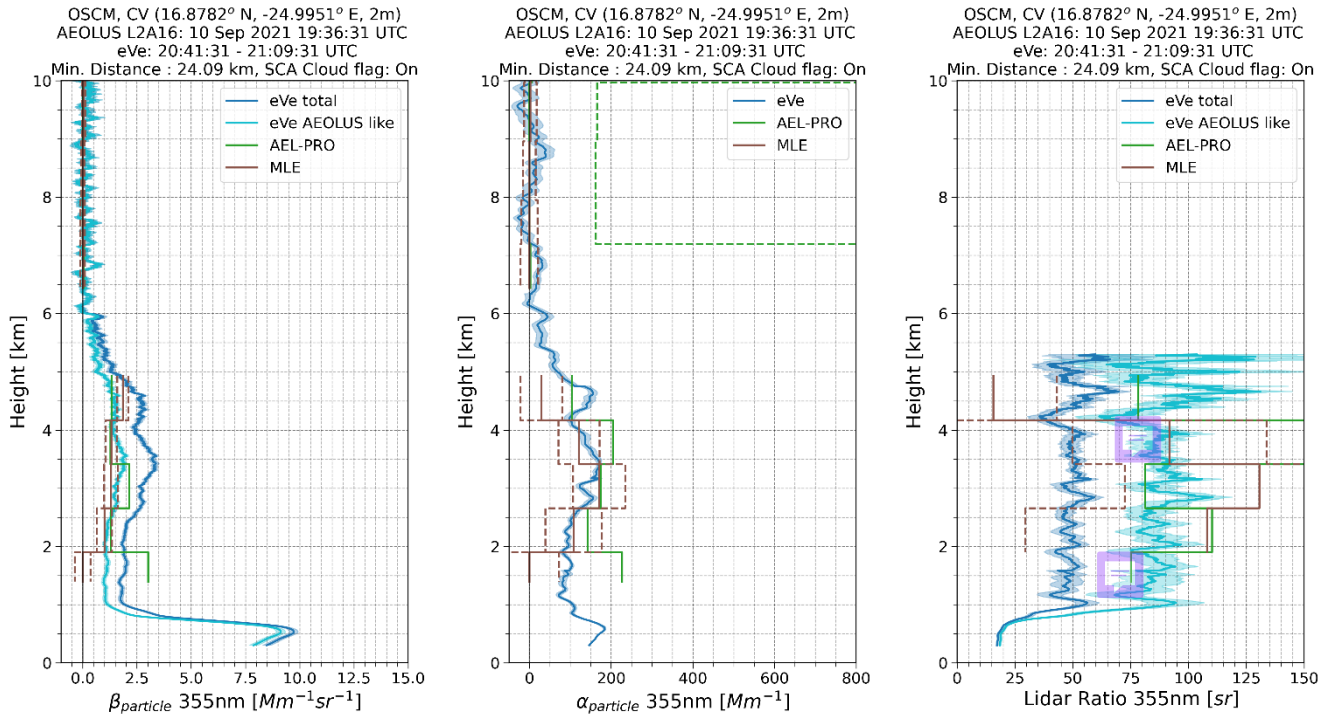
Figure 4: Comparison of the cloud masked Aeolus L2A profiles as obtained from the optimal estimation algorithms AEL–PRO
380 **(green) and MLE (brown) with Baseline 16 against eVe L2 lidar products for the Aeolus overpass on 10 September 2021. The averaged eVe lidar profiles of the Aeolus like particle backscatter (Aeolus like β$_{particle}$), particle extinction coefficient (α$_{particle}$), and Aeolus like lidar ratio were retrieved within the timeframe 20:41 to 21:09 UTC. The uncertainty of retrievals is denoted with shaded regions in the eVe profiles and with dashed lines in the Aeolus profiles.**

3.2 Statistical Analysis

385 A statistical analysis has been performed using the 14 eVe – Aeolus collocations aiming to assess the overall performance of Aeolus during the ASKOS period. For the statistical analysis, the eVe profiles have been rescaled to the Aeolus binning resolution to account for the fact that the number of the vertical bins provided from Aeolus is fixed but the height that corresponds to each bin changes along the orbit (for each orbit's BRC) and from orbit to orbit. Moreover, an upper threshold in the retrieved statistical uncertainty of each eVe profile (β_{uncer}< 1 Mm^{-1}sr^{-1}, α_{uncer}< 50 Mm^{-1}, LR_{uncer}< 50 sr) has been
390 applied for excluding height bins with high statistical uncertainty (e.g. regions with low signal-to-noise ratio) from the analysis. Then, for each L2A product the vertically resolved biases have been calculated and then sorted in classes based on three different parameters that can be related to the height, the thickness of the measured air masses, and the load of the suspended particles which can affect the lidar retrievals. For the latter component, the main dependencies are the following: i) the bin height since the retrieved optical properties are a function of the height, ii) the overlying total optical depth, and iii) the
395 scattering ratio (i.e., the total-to-molecular backscatter ratio). The statistical metrics that have been calculated per classes for the cloud masked Aeolus L2A profiles and are provided in Table 1 including the mean bias (MB) and standard deviation (STD)

and the root mean square error (RMSE). Based on the literature review from Walther and Moore, (2005), the MB of each distribution corresponds to the systematic error for each class, the STD is representative of the random error which can be due either to noise in the data or to natural variability since the ground-based and satellite lidars are not probing the same air mass,

400   and the RMSE corresponds to the overall magnitude of error. The metrics calculated from a class sample with N<5 are not taken into consideration in the results. The eVe profiles that have been used as reference in the statistical metrics are the Aeolus-like particle backscatter coefficient, the particle extinction coefficient, and the Aeolus-like lidar ratio.

Table 1: The metrics of mean bias, standard deviation, and root mean square error where n is the sample size, x_i is the measured value from Aeolus, $x_{ref,i}$ is the reference/true value from eVe, b_i is the calculated bias ($b_i = x_i - x_{ref.i}$), $\bar{b}$ is the mean bias, and Σ is

405   **the summation formula.**

Metric	Formula
Mean Bias (MB)	$MB = \frac{1}{n}\sum_{i=1}^{n}(x_i - x_{ref.i})$
Standard Deviation (STD)	$STD = \sqrt{\frac{1}{n-1}\sum_{i=1}^{n}\left(b_i - \bar{b}\right)^2}$
Root Mean Square Error (RMSE)	$RMSE = \sqrt{\frac{1}{n-1}\sum_{i=1}^{n}\left(x_i - x_{ref.i}\right)^2}$

In the classification parameters, the scattering ratio has been calculated for each overpass and Aeolus bin using the eVe particle backscatter coefficient profiles rescaled to the Aeolus bins and a molecular backscatter coefficient estimated using temperature and pressure profiles from the U.S. standard atmosphere model (initialized with P=1005 hPa and T=297.15 K at 84 m). The

410   overlying optical depth (OOD) has been calculated for each Aeolus bin by integrating the total (particle and molecular) extinction coefficient from the topmost Aeolus bin downwards to each successive bin. The particle extinction coefficient used for the OOD calculation has been calculated using the rescaled eVe particle backscatter coefficient multiplied by a mean lidar ratio value of 45.4 sr that has been calculated from the eVe lidar ratio profiles in the height range $2 - 4$ km. The molecular extinction coefficient profiles have been estimated relying on the U.S. standard atmosphere model. To account also the

415   molecular extinction contribution in heights above the Aeolus topmost bin for the OOD calculation, an offset value has been considered that corresponds to overlying molecular optical depth from the upper altitude limit in U.S. standard atmosphere model (~ 85 km) until the topmost Aeolus height bin.

The results from the statistical analysis using eight altitude classes to group the biases between Aeolus and eVe Aeolus-like profiles are presented in Fig. 5 for the backscatter coefficient, in Fig. 6 for the extinction coefficient, and in Fig.7 for the lidar

420   ratio.
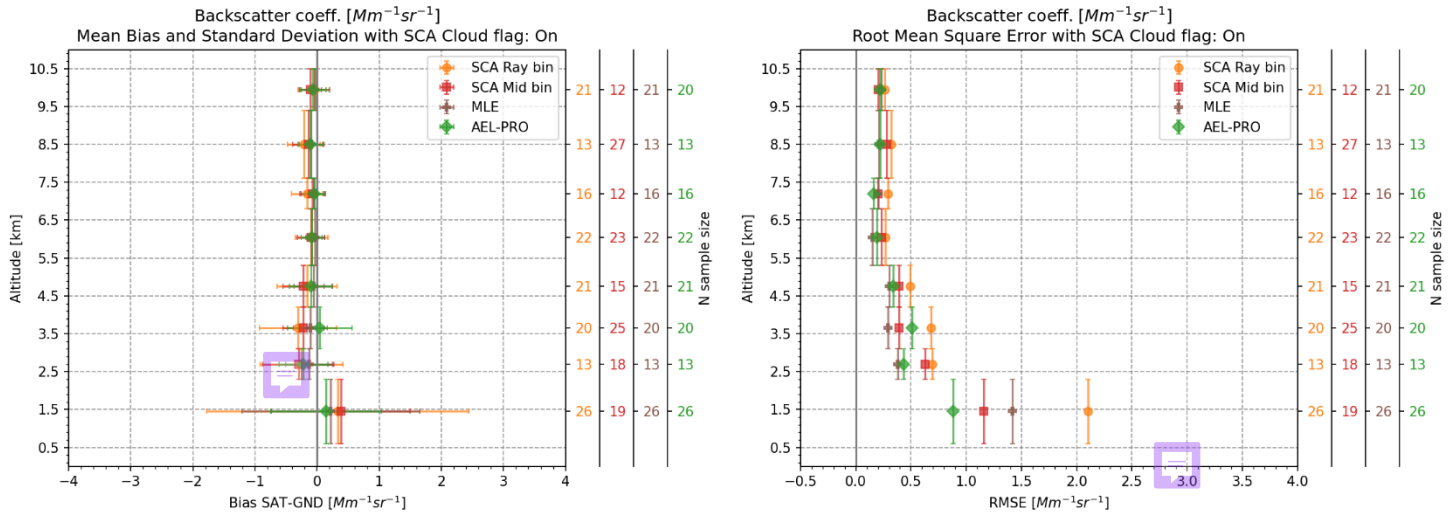
Figure 5: The Mean Bias and its Standard Deviation as error bars in the horizontal axis (left plot) and the Root Mean Square Error (right plot) of the Aeolus backscatter coefficient from SCA (–Rayleigh bin in orange circles; –Mid bin in red squares), AEL–PRO (green diamonds), and MLE (brown crosses) as a function of eight altitude classes. The error bars in the vertical axis corresponds to the classes' boundaries (0.6, 2.3, 3.1, 4.2, 5.3, 6.8, 7.6, 9.4, 10.5 km). The secondary y-axis indicates the sample size N per class for
425 **each algorithm. Metrics with N<5 are not taken into consideration.**

For the backscatter coefficient (Fig. 5), Aeolus tends to slightly overestimate the co-polar backscatter coefficient in the first altitude class (0.6 – 2.3 km) with the systematic error (MB) ± random error (STD) to be equal to 0.33 ± 2.07 Mm^{-1}sr^{-1} for the SCA–Rayleigh bin, 0.38 ± 1.09 Mm^{-1}sr^{-1} for the SCA–Mid bin, 0.14 ± 0.88 Mm^{-1}sr^{-1} for the AEL–PRO, and 0.22 ± 1.4 Mm^{-1}sr^{-1} for the MLE profiles. The corresponding overall error (RMSE) values in the first altitude class are 2.1 Mm^{-1}sr^{-1} for the

430 SCA–Rayleigh bin, 1.2 Mm^{-1}sr^{-1} for the SCA–mid bin, 0.88 Mm^{-1}sr^{-1} for the AEL–PRO, and 1.4 Mm^{-1}sr^{-1} for the MLE. In the rest altitude classes, negative MB values are observed indicating underestimation of the Aeolus (co-polar) backscatter coefficient. More specifically, in the height classes from 2.3 to 5.3 km where the dust particles mostly reside during ASKOS (Marinou et al., 2023), the systematic (MB) and random (STD) errors are up to -0.31 ± 0.61 Mm^{-1}sr^{-1} for SCA–Rayleigh bin, up to -0.3 ± 0.55 Mm^{-1}sr^{-1} for the SCA–Mid bin, up to -0.13 ± 0.36 Mm^{-1}sr^{-1} for the MLE, and up to -0.22 ± 0.37 Mm^{-1}sr^{-1} for

435 the AEL–PRO, whereas, in the height classes above 5.3 km the systematic and random errors are up to -0.21 ± 0.25 Mm^{-1}sr^{-1} for the SCA–Rayliegh bin, up to -0.14 ± 0.24 Mm^{-1}sr^{-1} for the SCA–Mid bin, up to -0.1 ± 0.18 Mm^{-1}sr^{-1} for the MLE, and up to -0.07 ± 0.21 Mm^{-1}sr^{-1} for the AEL–PRO. ==Finally, the overall error shows similar values with the random error in all classes== for all algorithms, with their difference to be observed in the second decimal place, indicating that the overall error is primarily driven by random variability rather than systematic bias. Overall, a decreasing trend is observed in the systematic, random, and overall errors with increasing of the height with the overall error decreasing from 2.1 to 0.26 Mm^{-1}sr^{-1} for the SCA–

440 Rayleigh bin, from 1.2 to 0.2 Mm^{-1}sr^{-1} for the SCA–Mid bin, from 0.88 to 0.22 Mm^{-1}sr^{-1} for the AEL–PRO, and from 1.4 to 0.23 Mm^{-1}sr^{-1} for the MLE. ==A decreasing trend of the errors with altitude increase is also reported in past related studies== (Baars et al., 2021; Abril-Gago et al., 2022; Gkikas et al., 2023).
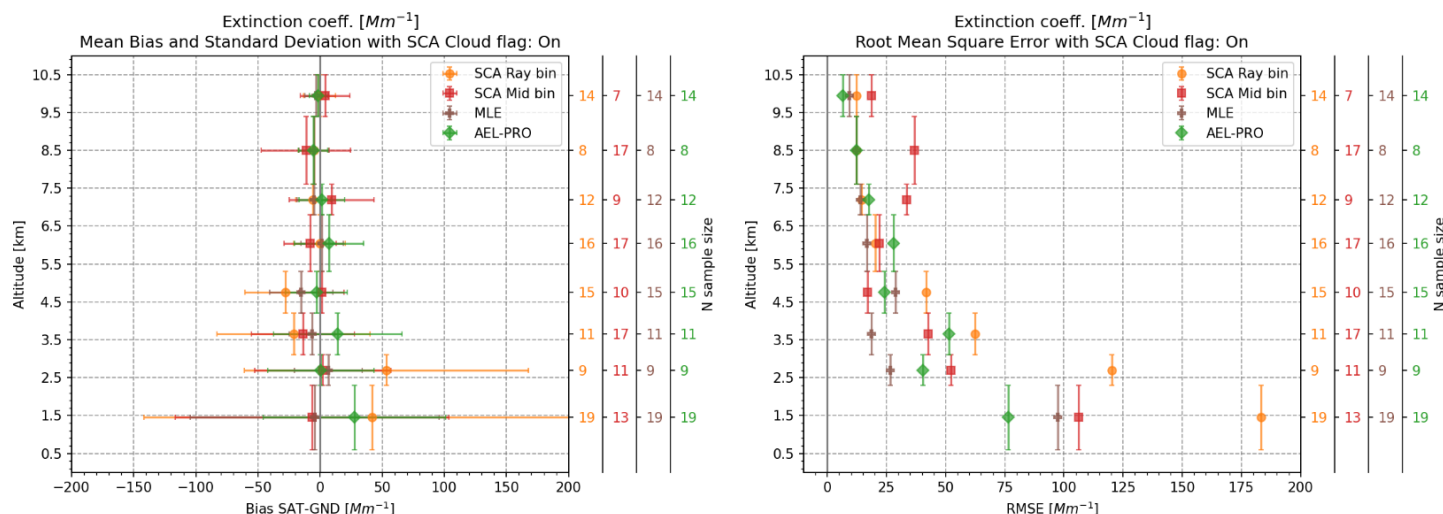
445 **Figure 6: The Mean Bias and its Standard Deviation as error bars in the horizontal axis (left plot) and the Root Mean Square Error (right plot) of the Aeolus extinction coefficient from SCA (–Rayleigh bin in orange circles; –Mid bin in red squares), AEL–PRO (green diamonds), and MLE (brown crosses) as a function of eight altitude classes. The error bars in the vertical axis corresponds to the classes' boundaries (0.6, 2.3, 3.1, 4.2, 5.3, 6.8, 7.6, 9.4, 10.5 km). The secondary y-axis indicates the sample size N per class for each algorithm. Metrics with N<5 are not taken into consideration.**

450 The statistical analysis into eight altitude classes for the extinction coefficient (Fig. 6) reveals higher errors variability due to the noisier Aeolus retrievals for the extinction coefficient than the co-polar backscatter coefficient. Unlike the backscatter coefficient, the systematic errors in the extinction coefficient does not follow a common behavior among the Aeolus algorithms: the SCA–Rayleigh bin overestimates the extinction coefficient up to 53 Mm^{-1} within the height ranges from 0.6 to 3.1 km and underestimates it up to 28 Mm^{-1} from 3.1 to 10.5 km, the AEL–PRO overestimates the extinction up to 27 Mm^{-1}

455 in the classes covering the heights 0.6 – 4.2 km with a systematic error variability from -6 to 7 Mm^{-1} in the rest altitude classes, while the SCA–Mid bin and the MLE demonstrate a systematic error variability from -14 to 9 Mm^{-1} and from -15 to 7 Mm^{-1}, respectively, without profound trend of under or overestimation. Moreover, for both the overall and the random error, which have similar values in all classes with RMSE and STD to differ by few Mm^{-1}, the highest values are observed in the first altitude class (0.6 – 2.3 km), namely overall errors equal to 183 Mm^{-1} for the SCA–Rayleigh bin, 106 Mm^{-1} for the SCA–Mid

460 bin, 77 Mm^{-1} for the AEL–PRO, and 97 Mm^{-1} for the MLE which are decreased (mostly gradually) with increasing of altitude from 120 to 12 Mm^{-1} for the SCA–Rayleigh bin, from 52 to 19 Mm^{-1} for the SCA–Mid bin, from 51 to 7 Mm^{-1} for the AEL–PRO, and from 29 to 9 Mm^{-1} for the MLE. In lidar ratio (Fig.7) the corresponding systematic, random, and overall errors for the eight altitude classes present large values and variability due to high levels of noise in the Aeolus lidar ratio retrievals from all the available algorithms. However, the MLE algorithm seems to be in better agreement with the corresponding eVe Aeolus

465 like lidar ratio retrievals in the heights where aerosols are more frequently detected (0.6 – 5.3 km) since the systematic and the overall error reach values up to 25 sr and 33 sr, respectively, followed by the AEL–PRO (MB up to 43 sr and RMSE up to 54

sr) and then the SCA (MB up to 266 sr and RMSE up to 771 sr). Similar to the backscatter and extinction coefficients, the random and overall error values differ only by few sr also for the lidar ratio in all altitude classes indicating that the random variability is the main driver for the overall error for the three Aeolus L2A retrievals (backscatter, extinction, and lidar ratio).
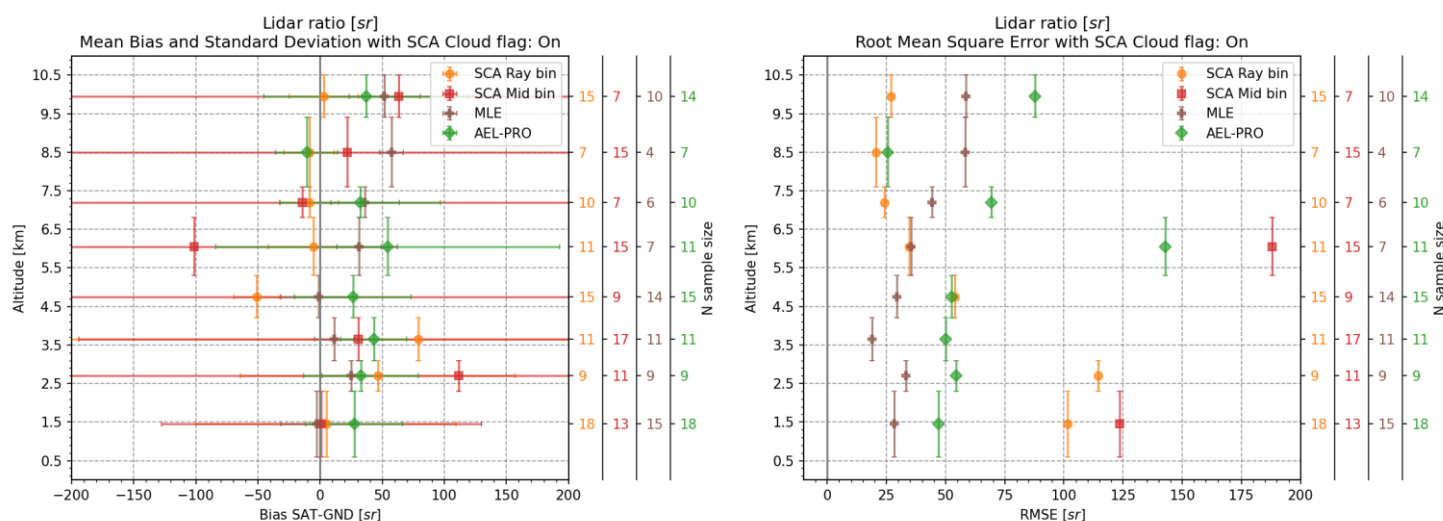
Figure 7: The Mean Bias and its Standard Deviation as error bars in the horizontal axis (left plot) and the Root Mean Square Error (right plot) of the Aeolus lidar ratio from SCA (–Rayleigh bin in orange circles; –Mid bin in red squares), AEL–PRO (green diamonds), and MLE (brown crosses) as a function of eight altitude classes. The error bars in the vertical axis corresponds to the classes' boundaries (0.6, 2.3, 3.1, 4.2, 5.3, 6.8, 7.6, 9.4, 10.5 km). The secondary y-axis indicates the sample size N per class for each algorithm. Metrics with N<5 are not taken into consideration.

The results from the statistical analysis using six OOD classes and four scattering ratio classes using the biases between Aeolus and eVe Aeolus like profiles falling within the height range 0.5 – 10.5 km are presented herein, for the backscatter coefficient in Figures 8 and 9, respectively; for the extinction coefficient in Figures 10 and 11, respectively; and for the lidar ratio in figures 12 and 13, respectively. This extra analysis using the overlying optical depth and the scattering ratio classes has been applied to the data for providing additional insights in the behavior of the biases under different atmospheric and aerosol loads.

In general, the overlying optical depth increases as we reach lower heights (i.e. thicker air masses) in the atmosphere where higher scattering ratio values are typically encountered due to presence of aerosols, as such, the attenuation of the Aeolus laser beam is expected to be higher in the lower heights leading to larger discrepancies (random errors; reduction of signal-to-noise ratio) of the Aeolus profiles against the reference ones acquired by eVe. Indeed, the statistical results from the OOD and scattering ratio classes indicate that the overall errors, which are primarily driven by the random variability since RMSE and STD have again similar values, increase with increasing of the OOD and the scattering ratio.

Moreover, for the backscatter coefficient (Figures 8 and 9), an underestimation tendency is observed in the classes with OOD less than 0.73 (Fig. 8) since the systematic error ranges from -0.22 to 0.07 Mm^{-1}sr^{-1} for the SCA–Rayleigh bin, from -0.27 to -0.05 Mm^{-1}sr^{-1} for the SCA–Mid bin, from -0.14 to -0.02 Mm^{-1}sr^{-1} for the AEL–PRO with the exception of a positive MB of 0.12 Mm^{-1}sr^{-1} in the OOD class 0.15 – 0.25, and from -0.13 to -0.04 Mm^{-1}sr^{-1} for the MLE with the exception of a positive MB

490 of 0.14 Mm^{-1}sr^{-1} in the OOD class 0.15 – 0.25. The overall errors in the classes with OOD from 0.25 to 0.73 increase with increasing OOD ranging from 0.22 to 0.7 Mm^{-1}sr^{-1} for the SCA–Rayleigh bin, from 0.2 to 0.57 Mm^{-1}sr^{-1} for the SCA–Mid bin, from 0.17 to 0.49 Mm^{-1}sr^{-1} for the AEL–PRO, and from 0.16 to 0.49 Mm^{-1}sr^{-1} for the MLE. The OOD class 0.73 – 1.19 is the class with the maximum systematic and overall error values with the corresponding MB and RMSE values to be 0.29 Mm^{-1}sr^{-1} and 2.13 Mm^{-1}sr^{-1} for the SCA–Ray bin, 0.17 and 1.06 Mm^{-1}sr^{-1} for the SCA–Mid bin, 0.13 and 0.9 Mm^{-1}sr^{-1} for the AEL–

495 PRO, and 0.29 and 1.38 Mm^{-1}sr^{-1} for the MLE, respectively, indicating slight overestimation of the backscatter in the lower heights where the overlying optical depth is high. Complementary, the mean biases calculated within the different scattering ratio classes (Fig. 9) range from -0.17 to 0.01 Mm^{-1}sr^{-1} for the SCA–Rayleigh bin, from -0.18 to -0.02 Mm^{-1}sr^{-1} for the SCA–Mid bin, from -0.07 to -0.01 Mm^{-1}sr^{-1} for the AEL–PRO, and from -0.11 to 0.08 Mm^{-1}sr^{-1} for the MLE. Similar absolute values for the STD (random error) and RMSE (overall error) are observed when using the scattering ratio classes. Moreover, for all

500 algorithms the overall error increases with increase of the scattering ratio, e.g. from 0.34 to 1.76 Mm^{-1}sr^{-1} for the SCA–Rayleigh bin, from 0.17 to 0.75 Mm^{-1}sr^{-1} for the SCA–Mid bin, from 0.14 to 0.72 Mm^{-1}sr^{-1} for the AEL–PRO, and from 0.1 to 1.16 Mm^{-1}sr^{-1} for the MLE.
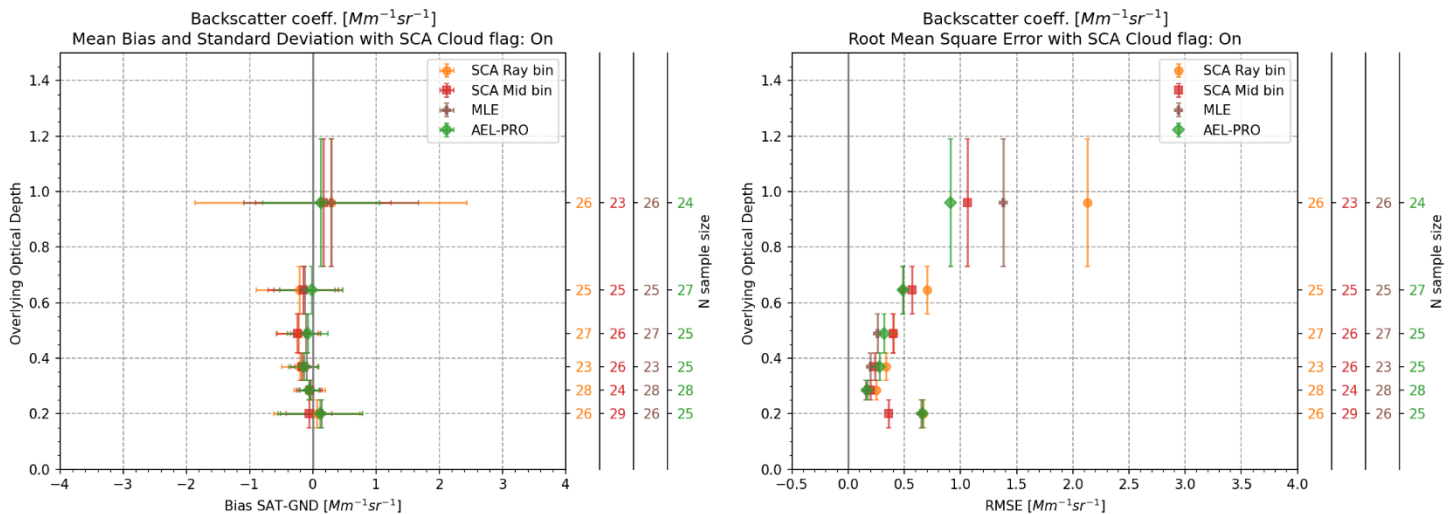
Figure 8: The Mean Bias and its Standard Deviation (left plot) and the Root Mean Square Error (right plot) of the Aeolus backscatter coefficient from SCA (–Rayleigh bin in orange circles; –Mid bin in red squares), AEL–PRO (green diamonds), and MLE (brown
505 **crosses) as a function of six OOD classes. The error bars in the vertical axis corresponds to the classes' boundaries: 0.15, 0.25, 0.32, 0.42, 0.56, 0.73, 1.19. The secondary y-axis indicates the sample size N per class for each algorithm.**
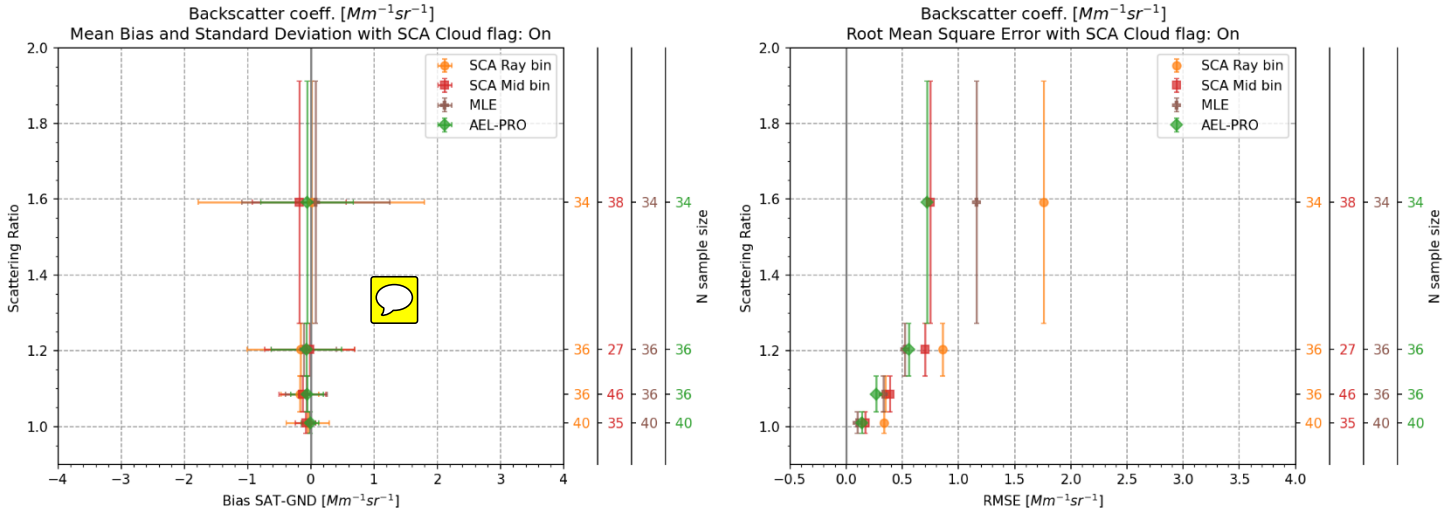
Figure 9: The Mean Bias and its Standard Deviation (left plot) and the Root Mean Square Error (right plot) of the Aeolus backscatter coefficient from SCA (–Rayleigh bin in orange circles; –Mid bin in red squares), AEL–PRO (green diamonds), and MLE (brown crosses) as a function of four scattering ratio classes. The error bars in the vertical axis corresponds to the classes' boundaries: 0.98, 1.038, 1.13, 1.27, 1.91. The secondary y-axis indicates the sample size N per class for each algorithm.

For the extinction coefficient (Figures 10 and 11), similar behavior as for the backscatter coefficient is observed for the SCA–Rayleigh and –Mid bin and the MLE algorithms but with larger discrepancies due to the noisier extinction retrievals from Aeolus, i.e., underestimation tendency in the OOD classes with OOD values up to 0.73. More specifically, for SCA the systematic error for the extinction mainly increases with increasing OOD from -0.1 to -16 Mm^{-1} and the overall error increases from 17 to 82 Mm^{-1} for the Rayleigh bin, while for the Mid bin the systematic error increases from -2 to -16 Mm^{-1} and the overall error ranges from 21 to 56 Mm^{-1}. In the OOD class 0.73 – 1.19 the SCA systematic and overall errors are found to be 65 and 199 Mm^{-1} in the Rayleigh bin resolution and 8 and 101 Mm^{-1} in the Mid bin resolution, respectively, indicating overestimation of the extinction in height bins with significant atmospheric load in the overlying layers. For the MLE retrievals, the systematic error increases from -0.6 to -21 Mm^{-1} and the overall error ranges from 12 to 46 Mm^{-1} when the data are sorted into classes with OOD less than 0.73, while in the OOD class 0.73 – 1.19 the systematic error is 11 Mm^{-1} and the overall error is 95 Mm^{-1}. In AEL–PRO, the systematic error for the extinction ranges from -1 to 20 Mm^{-1} and the overall error ranges from 13 to 77 Mm^{-1}. Again, similar behavior of increasing systematic, random, and overall errors with increase of the OOD is observed also with increase of the scattering ratio.
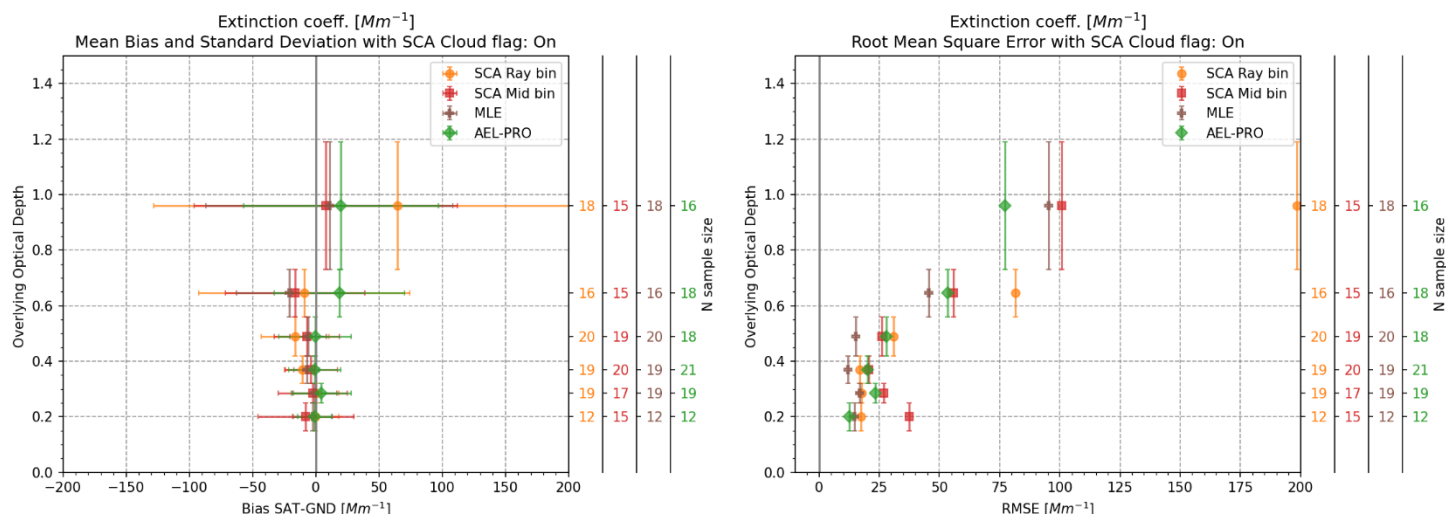
Figure 10: The Mean Bias and its Standard Deviation (left plot) and the Root Mean Square Error (right plot) of the Aeolus extinction
coefficient from SCA (–Rayleigh bin in orange circles; –Mid bin in red squares), AEL–PRO (green diamonds), and MLE (brown
crosses) as a function of six OOD classes. The error bars in the vertical axis corresponds to the classes' boundaries: 0.15, 0.25, 0.32,
0.42, 0.56, 0.73, 1.19. The secondary y-axis indicates the sample size N per class for each algorithm.
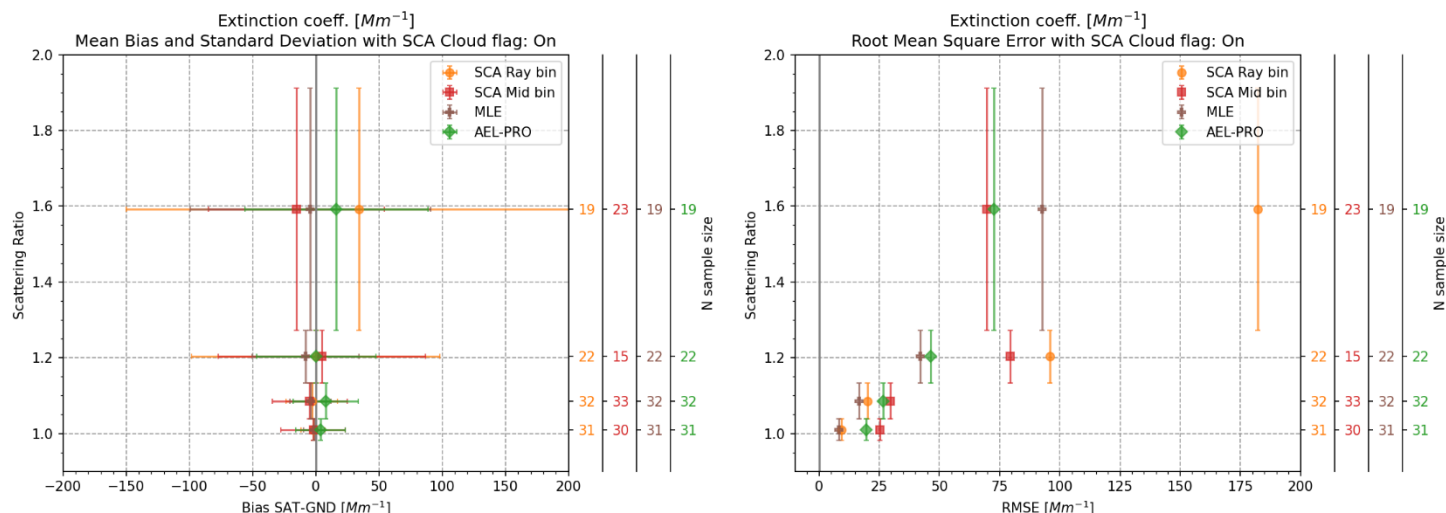
Figure 11: The Mean Bias and its Standard Deviation (left plot) and the Root Mean Square Error (right plot) of the Aeolus extinction
coefficient from SCA (–Rayleigh bin in orange circles; –Mid bin in red squares), AEL–PRO (green diamonds), and MLE (brown
crosses) as a function of four scattering ratio classes. The error bars in the vertical axis corresponds to the classes' boundaries: 0.98,
1.038, 1.13, 1.27, 1.91. The secondary y-axis indicates the sample size N per class for each algorithm.

For the lidar ratio (Figures 12 and 13), the noisy Aeolus profiles result in large discrepancies in the systematic, random, and
overall errors for the OOD and the scattering ratio classes. Indicatively, the overall error, which has similar to values to the
random error, ranges among the six OOD classes from 25 to 275 sr for the SCA–Rayleigh bin, from 70 to 581 sr for the SCA–
Mid bin, from 36 to 147 sr for the AEL–PRO, and from 27 to 49 sr for the MLE. Here, opposite to the backscatter and extinction

coefficients, better agreement between the Aeolus and the eVe Aeolus like lidar ratio profiles seems to be observed in cases with high atmospheric load (OOD 0.73 – 1.19 and scattering ratio 1.27 – 1.9) with the systematic and the overall errors in the OOD class 0.73 – 1.19 to be 11 sr and 106 sr for the SCA–Rayleigh bin, -9 sr and 70 sr for the SCA–Mid bin, 17 sr and 36 sr for the AEL–PRO, and 2 sr and 32 sr for the MLE, respectively. Moreover, the higher values of the overall error for the Aeolus

540   lidar ratio from MLE and AEL–PRO are obtained in the classes with lower atmospheric loads (OOD 0.15 – 0.25 and scattering ratio 0.98 – 1.04), while for the SCA lidar ratio the overall error has higher values in the classes with higher atmospheric loads (OOD 0.73 – 1.19 and scattering ratio 1.27 – 1.9). Nevertheless, the above findings for the lidar ratio are overshadowed by the large error values and variability in the lidar ratio statistics.
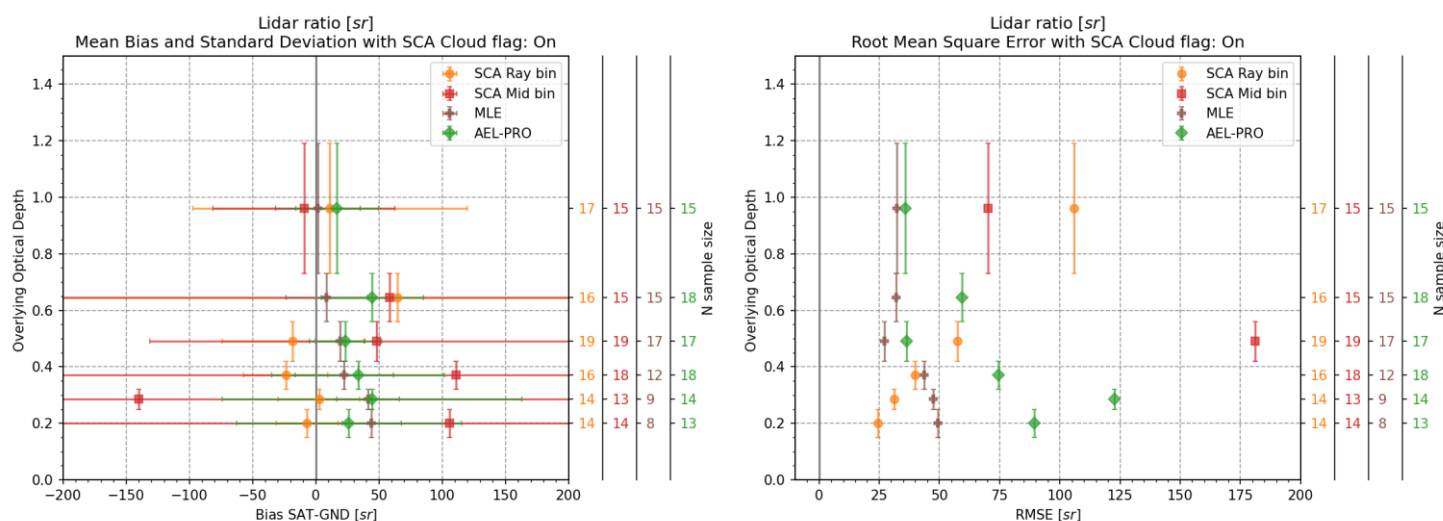
Figure 12: The Mean Bias and its Standard Deviation (left plot) and the Root Mean Square Error (right plot) of the Aeolus lidar
545   **ratio from SCA (–Rayleigh bin in orange circles; –Mid bin in red squares), AEL–PRO (green diamonds), and MLE (brown crosses) as a function of six OOD classes. The error bars in the vertical axis corresponds to the classes' boundaries: 0.15, 0.25, 0.32, 0.42, 0.56, 0.73, 1.19. The secondary y-axis indicates the sample size N per class for each algorithm.**
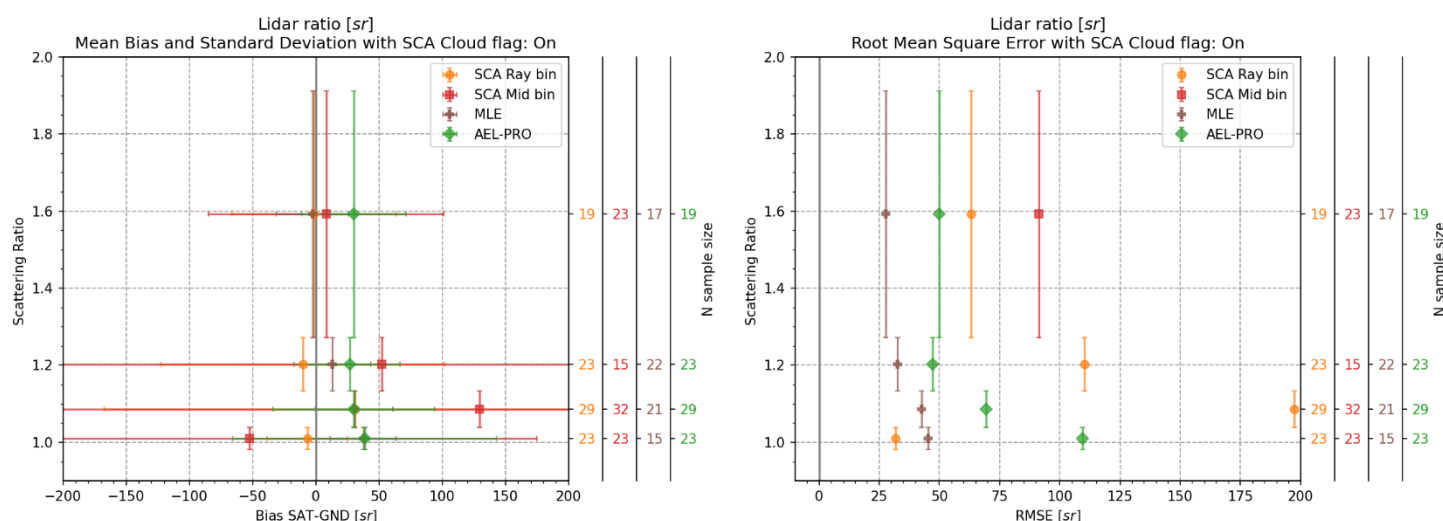
Figure 13: The Mean Bias and its Standard Deviation (left plot) and the Root Mean Square Error (right plot) of the Aeolus lidar
ratio from SCA (–Rayleigh bin in orange circles; –Mid bin in red squares), AEL–PRO (green diamonds), and MLE (brown crosses)
as a function of four scattering ratio classes. The error bars in the vertical axis corresponds to the classes' boundaries: 0.98, 1.038,
1.13, 1.27, 1.91. The secondary y-axis indicates the sample size N per class for each algorithm.

4. Conclusions

The eVe lidar has been deployed in the ASKOS/JATAC campaign in Cabo Verde with the main aim of providing reference
measurements for the validation of the Aeolus L2A products. Leveraging 14 collocated observations between eVe and Aeolus,
the validation study evaluates the performance of the SCA, MLE, and AEL–PRO algorithms in retrieving the Aeolus L2A
aerosol optical properties focusing on an environment with desert dust, marine aerosols, and dust mixtures as the predominant
aerosol types. The Aeolus L2A profiles used in the analysis are masked from the cloud contaminated bins based on the cloud
flagging from the SCA algorithm.

The one-by-one comparison between eVe and Aeolus L2A profiles performed at a pure dust case reveals generally good
agreement for the (co-polar) particle backscatter coefficient within the height range 2.5 – 5.5 km where the desert dust particles
are observed. Among the algorithms, the MLE algorithm achieves the smallest bias of 0.41 $Mm^{-1}sr^{-1}$, followed by AEL–PRO
with 0.6 $Mm^{-1}sr^{-1}$, while the SCA–Mid bin (0.56 $Mm^{-1}sr^{-1}$) shows improved performance over the SCA–Rayleigh bin (1.2 $Mm^{-1}sr^{-1}$). For the particle extinction coefficient, the SCA algorithm exhibits higher biases in the extinction, with maximum absolute
values reaching 124 Mm^{-1} for the SCA–Mid bin and 273 Mm^{-1} for the SCA–Rayleigh bin. The MLE and AEL–PRO optimal
estimator algorithms demonstrate improved accuracy, with biases ranging from 13 to 99 Mm^{-1} for the MLE and 24 to 55 Mm^{-1} for the AEL–PRO. Notably, the lidar ratio shows significant noise across all algorithms. For the lidar ratio from SCA
algorithm, absolute biases exceed 30 sr and reach up to 127 sr inside the dust layer. Although, the lidar ratio from MLE and

570 AEL–PRO algorithms performs better with smaller biases at certain heights, e.g., biases of 4 sr at ~3.7 km for MLE and 11 sr at ~3 km and ~4.5 km for AEL–PRO, the agreement remains sporadic.

Additionally, a statistical analysis has been performed on the 14 eVe – Aeolus collocations offering a broader perspective on systematic and random errors. The mean bias (MB), standard deviation (STD) and root mean square error (RMSE) have been calculated across different classes based on the altitude, the overlying optical depth (OOD), and the scattering ratio. For the backscatter coefficient which is the most accurate Aeolus L2A product ~~among the extinction coefficient and the lidar ratio~~, the

575 biases decrease with increase of altitude, reflecting improved performance in higher altitudes as already reported in similar validation studies (Baars et al., 2021; Abril-Gago et al., 2022; Gkikas et al., 2023). In the 2.3 – 5.3 km range where the dust particles mostly reside during ASKOS (Marinou et al., 2023), the systematic errors (MB) reached values up to -0.31 $Mm^{-1}sr^{-1}$ (SCA–Rayleigh bin), -0.3 $Mm^{-1}sr^{-1}$ (SCA–Mid), -0.13 $Mm^{-1}sr^{-1}$ (MLE), and -0.22 $Mm^{-1}sr^{-1}$ (AEL–PRO), indicating slight underestimation of the co-polar backscatter coefficient from Aeolus with corresponding overall error (RMSE) values up to 0.7

580 $Mm^{-1}sr^{-1}$ for the SCA, and 0.4 $Mm^{-1}sr^{-1}$ for the MLE and 0.5 $Mm^{-1}sr^{-1}$ for the AEL–PRO. However, the overall errors increased significantly in the lower atmospheric layers, particularly in the 0.6 – 2.3 km range, where the RMSE reached the 2 $Mm^{-1}sr^{-1}$ for the SCA–Rayleigh, the 1.2 $Mm^{-1}sr^{-1}$ for the SCA–Mid bin, the 1.4 $Mm^{-1}sr^{-1}$ for the MLE, and the 0.9 $Mm^{-1}sr^{-1}$ for the AEL–PRO. The extinction coefficient exhibited larger discrepancies and variability compared to the backscatter coefficient due to the noisier retrievals from Aeolus. In the 0.6 – 2.3 km range, the overall errors reached values up to 183 Mm^{-1} (SCA–Rayleigh),

585 106 Mm^{-1} (SCA–Mid), 97 Mm^{-1} (MLE), and 77 Mm^{-1} (AEL–PRO), while in the rest altitude classes the overall errors reduced to 12 Mm^{-1} (SCA–Rayleigh), 19 Mm^{-1} (SCA–Mid), 9 Mm^{-1} (MLE), and 7 Mm^{-1} (AEL–PRO). The MLE algorithm demonstrated the most consistent performance with overall errors ranging from 9 to 29 Mm^{-1}, while the SCA algorithms showed larger overall error variations, from 12 to 120 Mm^{-1}. The lidar ratio remains the noisiest product, with errors compounded in both systematic and random metrics. However, the MLE demonstrates improved performance with overall

590 errors up to 33 sr, followed by the AEL–PRO with 54 sr and the SCA with 771 sr (–Mid bin) in the heights where the aerosols are more frequently detected. Moreover, the discrepancies between eVe and Aeolus profiles generally increase in lower altitudes where higher OOD and scattering ratio values are obtained, reflecting the higher atmospheric variability (e.g. PBL inhomogeneities) that is typically encountered in lower altitudes as well as the greater aerosol loads at lower altitudes that lead to enhanced laser beam attenuation for Aeolus (i.e. higher noise levels). For the backscatter coefficient, underestimations

595 dominate in lower OOD ~~classes where the systematic error can reach up to -0.27~~ $Mm^{-1}sr^{-1}$ ~~for the SCA profiles and -0.14~~ $Mm^{-1}sr^{-1}$ ~~for the profiles from the optimal estimators (MLE and AEL–PRO) with overall errors up to 0.7~~ $Mm^{-1}sr^{-1}$ ~~for the SCA and up to 0.49~~ $Mm^{-1}sr^{-1}$ ~~for the optimal estimators~~. In the class with the highest overlying optical depth (OOD 0.73 – 1.19) the overall errors are in the order of 0.9 $Mm^{-1}sr^{-1}$ for AEL–PRO, 1.4 $Mm^{-1}sr^{-1}$ for SCA–Mid bin and MLE, and 2.1 $Mm^{-1}sr^{-1}$ for the SCA–Rayleigh bin, since they increase with increase of the overlying optical depth. The extinction coefficient from Aeolus

600 is underestimated by the SCA and MLE algorithms in the classes with OOD less than 0.73 where the corresponding systematic errors were found to be up to -21 Mm^{-1} and overall errors up to 82 Mm^{-1} (SCA) and 46 Mm^{-1} (MLE), whereas the AEL–PRO

systematic errors range from -1 to 19 Mm^{-1} with overall errors up to 54 Mm^{-1}. In the highest aerosol load class (OOD 0.73 – 1.19) the systematic errors are 20 Mm^{-1} for the AEL–PRO, 11 Mm^{-1} for the MLE, and 65 Mm^{-1} and 7 Mm^{-1} for the SCA–Rayleigh and –Mid bin, respectively, with corresponding overall errors of 77 Mm^{-1} for the AEL–PRO, 95 Mm^{-1} for the MLE, and 199 Mm^{-1} and 101 Mm^{-1} for the SCA–Rayleigh and –Mid bin, respectively. For the lidar ratio, the discrepancies are pronounced due to noise in the Aeolus profiles, with overall error values ranging from 25 to 581 sr across algorithms with MLE having the lower reported overall error of 27 sr followed by the AEL–PRO with 36 sr. Notably, the best agreement between Aeolus and eVe profiles for the lidar ratio occurs in the class with the highest overlying atmospheric load (OOD 0.73 – 1.19) where MLE achieved systematic and overall errors of 2 sr and 32 sr, respectively, followed by AEL–PRO with 17 sr and 36 sr. The SCA profiles showed significantly higher discrepancies, with overall error values exceeding the 70 sr. Similar trends for each product are observed also in the analysis using the scattering ratio classes.

Overall, the results underline the strengths of the optimal estimators (MLE and AEL–PRO) while the SCA algorithm could be further improved, particularly in the retrieval of the extinction and lidar ratio products. The MLE algorithm demonstrates consistent performance across metrics, reducing both systematic and random errors, closely followed by the AEL–PRO algorithm which performs well particularly for the extinction coefficient retrievals. For SCA, the –Mid bin profiles outperform the corresponding –Rayleigh bin reflecting the reduction of the bias and noise levels in the L2A profiles when averaging the values from two consecutive height bins. The systematic errors in all algorithms are overshadowed by the random errors concluding that the discrepancies between eVe and Aeolus profiles are driven by the variability in atmospheric conditions and the inherent noise in Aeolus profiles, especially at lower altitudes where the aerosol layers reside.

Code Availability

The software code used in this work is available upon request

Data Availability

The reprocessed Aeolus L2A products with Baseline 16 are provided by the European Space Agency (ESA) Earth Explorer Program and are available from the online Aeolus Data Dissemination Facility (https://aeolus-ds.eo.esa.int/oads/access/collection/Level_2A_aerosol_cloud_optical_products_Reprocessed). The eVe dataset is publicly available through the ASKOS repository in the EVDC data portal (https://evdc.esa.int/publications/askos-campaign-dataset/).

Author Contribution

630 PP and NS collected and analysed the eVe lidar measurements shown herein with the support of SMI, DTQ, DDFA, GG in the operation of the eVe lidar. PP performed the analysis of the acquired measurements for the validation exercise on the Aeolus L2A products and the manuscript preparation with the support of NS, EM, AG, KV. DPD provided support in the processing of the Aeolus L2A products obtained from the AEL-PRO algorithm. VA supervised and directed the whole project. All authors provided critical feedback and helped shape the research, analysis and manuscript.

Competing Interests

635 Some authors are members of the editorial board of journal Atmospheric Measurement Techniques.

Acknowledgements

We acknowledge the financial support of the PANGEA4CalVal project (Grant Agreement 101079201) funded by the European Union ▢ ; the ASKOS project funded by the European Space Agency (contract No. 4000131861/20/NL/IA); the project

640 "PANhellenic infrastructure for Atmospheric Composition and climatE change" (MIS 5021516), implemented under the Action "Reinforcement of the Research and Innovation Infrastructure", funded by the Operational Programme "Competitiveness, Entrepreneurship and Innovation" (NSRF 2014-2020) and co-financed by Greece and the European Union (European Regional Development Fund); and the Stavros Niarchos Foundation. PP would like to thank D. Trapon for his support on the processing of the Aeolus data.

645 **References**

Abril-Gago, J., Guerrero-Rascado, J. L., Costa, M. J., Bravo-Aranda, J. A., Sicard, M., Bermejo-Pantaleón, D., Bortoli, D., Granados-Muñoz, M. J., Rodríguez-Gómez, A., Muñoz-Porcar, C., Comerón, A., Ortiz-Amezcua, P., Salgueiro, V., Jiménez-Martín, M. M., and Alados-Arboledas, L.: Statistical validation of Aeolus L2A particle backscatter coefficient retrievals over ACTRIS/EARLINET stations on the Iberian Peninsula, Atmos. Chem. Phys., 22, 1425–1451, https://doi.org/10.5194/acp-22-

650 1425-2022, 2022.

Abril-Gago, J., Ortiz-Amezcua, P., Bermejo-Pantaleón, D., Andújar-Maqueda, J., Bravo-Aranda, J. A., Granados-Muñoz, M. J., Navas-Guzmán, F., Alados-Arboledas, L., Foyo-Moreno, I., and Guerrero-Rascado, J. L.: Validation activities of Aeolus wind products on the southeastern Iberian Peninsula, Atmos. Chem. Phys., 23, 8453–8471, https://doi.org/10.5194/acp-23-8453-2023, 2023.

655 Amiridis, V., Kampouri, A., Gkikas, A., Misios, S., Gialitaki, A., Marinou, E., Rennie, M., Benedetti, A., Solomos, S., Zanis, P., Vasardani, O., Eleftheratos, K., Paschou, P., Georgiou, T., Scollo, S., Mona, L., Papagiannopoulos, N., Retscher, C.,

Parrinello, T., and Straume, A. G.: Aeolus winds impact on volcanic ash early warning systems for aviation, Sci. Rep., 13, 7531, https://doi.org/10.1038/s41598-023-34715-6, 2023.

Ansmann, A., Wandinger, U., Le Rille, O., Lajas, D., and Straume, A. G.: Particle backscatter and extinction profiling with the spaceborne high-spectral-resolution Doppler lidar ALADIN: methodology and simulations, Appl. Opt., 46, 6606, https://doi.org/10.1364/AO.46.006606, 2007.

Baars, H., Herzog, A., Heese, B., Ohneiser, K., Hanbuch, K., Hofer, J., Yin, Z., Engelmann, R., and Wandinger, U.: Validation of Aeolus wind products above the Atlantic Ocean, Atmos. Meas. Tech., 13, 6007–6024, https://doi.org/10.5194/amt-13-6007-2020, 2020.

Baars, H., Radenz, M., Floutsi, A. A., Engelmann, R., Althausen, D., Heese, B., Ansmann, A., Flament, T., Dabas, A., Trapon, D., Reitebuch, O., Bley, S., and Wandinger, U.: Californian Wildfire Smoke Over Europe: A First Example of the Aerosol Observing Capabilities of Aeolus Compared to Ground-Based Lidar, Geophys. Res. Lett., 48, e2020GL092194, https://doi.org/10.1029/2020GL092194, 2021.

Borne, M., Knippertz, P., Weissmann, M., Witschas, B., Flamant, C., Rios-Berrios, R., and Veals, P.: Validation of Aeolus L2B products over the tropical Atlantic using radiosondes, Atmos. Meas. Tech., 17, 561–581, https://doi.org/10.5194/amt-17-561-2024, 2024.

Córdoba-Jabonero, C., Sicard, M., Barreto, Á., Toledano, C., López-Cayuela, M. Á., Gil-Díaz, C., García, O., Carvajal-Pérez, C. V., Comerón, A., Ramos, R., Muñoz-Porcar, C., and Rodríguez-Gómez, A.: Fresh volcanic aerosols injected in the atmosphere during the volcano eruptive activity at the Cumbre Vieja area (La Palma, Canary Islands): Temporal evolution and vertical impact, Atmos. Environ., 300, 119667, https://doi.org/10.1016/J.ATMOSENV.2023.119667, 2023.

Donovan, D. P., van Zadelhoff, G.-J., and Wang, P.: Aeolus/ALADIN Algorithm Theoretical Basis Document Level 2A products AEL-FM, AEL-PRO, 64 pp., 2024a.

Donovan, D. P., van Zadelhoff, G.-J., and Wang, P.: The EarthCARE lidar cloud and aerosol profile processor (A-PRO): the A-AER, A-EBD, A-TC, and A-ICE products, Atmos. Meas. Tech., 17, 5301–5340, https://doi.org/10.5194/amt-17-5301-2024, 2024b.

Ehlers, F., Flament, T., Dabas, A., Trapon, D., Lacour, A., Baars, H., and Straume-Lindner, A. G.: Optimization of Aeolus' aerosol optical properties by maximum-likelihood estimation, Atmos. Meas. Tech., 15, 185–203, https://doi.org/10.5194/amt-15-185-2022, 2022.

Ern, M., Diallo, M. A., Khordakova, D., Krisch, I., Preusse, P., Reitebuch, O., Ungermann, J., and Riese, M.: The quasi-biennial oscillation (QBO) and global-scale tropical waves in Aeolus wind observations, radiosonde data, and reanalyses, Atmos. Chem. Phys., 23, 9549–9583, https://doi.org/10.5194/acp-23-9549-2023, 2023.

ESA: ADM-Aeolus science report, https://esamultimedia.esa.int/docs/EarthObservation/SP-1311ADM-Aeolus_Final.pdf, 2008.

Fehr, T., McCarthy, W., Amiridis, V., Baars, H., von Bismarck, J., Borne, M., Chen, S., Flamant, C., Marenco, F., and Knipperz, P.: The Joint Aeolus Tropical Atlantic Campaign 2021/2022 Overview–Atmospheric Science and Satellite

Validation in the Tropics, EGU23, https://doi.org/doi.org/10.5194/egusphere-egu23-7249, 2023.

Flamant, P., Cuesta, J., Denneulin, M.-L., Dabas, A., and Huber, D.: ADM-Aeolus retrieval algorithms for aerosol and cloud products, Tellus A, 60, 273–288, https://doi.org/10.1111/j.1600-0870.2007.00287.x, 2008.

Flamant, P., Lever, V., Martinet, P., Flament, T., Cuesta, J., Dabas, A., Olivier, M., Huber, D., Trapon, D., and Lacour, A.:
695   AE-TN-IPSL-GS-001 v6.0: ADM-Aeolus L2A Algorithm Theoretical Baseline Document., 95 pp., 2022.

Flament, T., Trapon, D., Lacour, A., Dabas, A., Ehlers, F., and Huber, D.: Aeolus L2A aerosol optical properties product: standard correct algorithm and Mie correct algorithm, Atmos. Meas. Tech., 14, 7851–7871, https://doi.org/10.5194/amt-14-7851-2021, 2021.

Gebauer, H., Floutsi, A. A., Haarig, M., Radenz, M., Engelmann, R., Althausen, D., Skupin, A., Ansmann, A., Zenk, C., and
700   Baars, H.: Tropospheric sulfate from Cumbre Vieja (La Palma) observed over Cabo Verde contrasted with background conditions: a lidar case study of aerosol extinction, backscatter, depolarization and lidar ratio profiles at 355, 532 and 1064 nm, Atmos. Chem. Phys., 24, 5047–5067, https://doi.org/10.5194/acp-24-5047-2024, 2024.

Gkikas, A., Proestakis, E., Amiridis, V., Kazadzis, S., Di Tomaso, E., Tsekeri, A., Marinou, E., Hatzianastassiou, N., and Pérez Garciá-Pando, C.: ModIs Dust AeroSol (MIDAS): A global fine-resolution dust optical depth data set, Atmos. Meas. Tech.,
705   14, https://doi.org/10.5194/amt-14-309-2021, 2021.

Gkikas, A., Gialitaki, A., Binietoglou, I., Marinou, E., Tsichla, M., Siomos, N., Paschou, P., Kampouri, A., Voudouri, K. A., Proestakis, E., Mylonaki, M., Papanikolaou, C.-A., Michailidis, K., Baars, H., Straume, A. G., Balis, D., Papayannis, A., Parrinello, T., and Amiridis, V.: First assessment of Aeolus Standard Correct Algorithm particle backscatter coefficient retrievals in the eastern Mediterranean, Atmos. Meas. Tech., 16, 1017–1042, https://doi.org/10.5194/amt-16-1017-2023, 2023.

710 Hagelin, S., Azad, R., Lindskog, M., Schyberg, H., and Körnich, H.: Evaluating the use of Aeolus satellite observations in the regional numerical weather prediction (NWP) model Harmonie--Arome, Atmos. Meas. Tech., 14, 5925–5938, https://doi.org/10.5194/amt-14-5925-2021, 2021.

Illingworth, A. J., Barker, H. W., Beljaars, A., Ceccaldi, M., Chepfer, H., Clerbaux, N., Cole, J., Delanoë, J., Domenech, C., Donovan, D. P., Fukuda, S., Hirakata, M., Hogan, R. J., Huenerbein, A., Kollias, P., Kubota, T., Nakajima, T., Nakajima, T.
715   Y., Nishizawa, T., Ohno, Y., Okamoto, H., Oki, R., Sato, K., Satoh, M., Shephard, M. W., Velázquez-Blázquez, A., Wandinger, U., Wehr, T., and Van Zadelhoff, G. J.: The EarthCARE Satellite: The Next Step Forward in Global Measurements of Clouds, Aerosols, Precipitation, and Radiation, Bull. Am. Meteorol. Soc., 96, 1311–1332, https://doi.org/10.1175/BAMS-D-12-00227.1, 2015.

Imaki, M., Takegoshi, Y., and Kobayashi, T.: Ultraviolet High-Spectral-Resolution Lidar with Fabry–Perot Filter for Accurate
720   Measurement of Extinction and Lidar Ratio, Jpn. J. Appl. Phys., 44, 3063–3067, https://doi.org/10.1143/JJAP.44.3063, 2005.

Kanitz, T., Lochard, J., Marshall, J., McGoldrick, P., Lecrenier, O., Bravetti, P., Reitebuch, O., Rennie, M., Wernham, D., and Elfving, A.: Aeolus first light: first glimpse, https://doi.org/10.1117/12.2535982, 2019.

Kiriakidis, P., Gkikas, A., Papangelis, G., Christoudias, T., Kushta, J., Proestakis, E., Kampouri, A., Marinou, E., Drakaki, E., Benedetti, A., Rennie, M., Retscher, C., Straume, A. G., Dandocsi, A., Sciare, J., and Amiridis, V.: The impact of using

725 assimilated Aeolus wind data on regional WRF-Chem dust simulations, Atmos. Chem. Phys., 23, 4391–4417, https://doi.org/10.5194/acp-23-4391-2023, 2023.

Liu, H., Garrett, K., Ide, K., Hoffman, R. N., and Lukens, K. E.: A statistically optimal analysis of systematic differences between Aeolus horizontal line-of-sight winds and NOAA's Global Forecast System, Atmos. Meas. Tech., 15, 3925–3940, https://doi.org/10.5194/amt-15-3925-2022, 2022.

730 Lolli, S., Delaval, A., Loth, C., Garnier, A., and Flamant, P. H.: 0.355-micrometer direct detection wind lidar under testing during a field campaign in consideration of ESA's ADM-Aeolus mission, Atmos. Meas. Tech., 6, 3349–3358, https://doi.org/10.5194/amt-6-3349-2013, 2013.

Lux, O., Lemmerz, C., Weiler, F., Marksteiner, U., Witschas, B., Rahm, S., Geiß, A., Schäfler, A., and Reitebuch, O.: Retrieval improvements for the ALADIN Airborne Demonstrator in support of the Aeolus wind product validation, Atmos. Meas. Tech.,

735 15, 1303–1331, https://doi.org/10.5194/amt-15-1303-2022, 2022.

Marinou, E., Paschou, P., Tsikoudi, I., Tsekeri, A., Daskalopoulou, V., Kouklaki, D., Siomos, N., Spanakis-Misirlis, V., Voudouri, K. A., Georgiou, T., Drakaki, E., Kampouri, A., Papachristopoulou, K., Mavropoulou, I., Mallios, S., Proestakis, E., Gkikas, A., Koutsoupi, I., Raptis, I. P., Kazadzis, S., Baars, H., Floutsi, A., Pirloaga, R., Nemuc, A., Marenco, F., Kezoudi, M., Papetta, A., Močnik, G., Díez, J. Y., Ryder, C. L., Ratcliffe, N., Kandler, K., Sudharaj, A., and Amiridis, V.: An Overview

740 of the ASKOS Campaign in Cabo Verde, Environ. Sci. Proc. 2023, Vol. 26, Page 200, 26, 200, https://doi.org/10.3390/ENVIRONSCIPROC2023026200, 2023.

Martin, A., Weissmann, M., Reitebuch, O., Rennie, M., Geiß, A., and Cress, A.: Validation of Aeolus winds using radiosonde observations and numerical weather prediction model equivalents, Atmos. Meas. Tech., 14, 2167–2183, https://doi.org/10.5194/amt-14-2167-2021, 2021.

745 Martin, A., Weissmann, M., and Cress, A.: Investigation of links between dynamical scenarios and particularly high impact of Aeolus on numerical weather prediction (NWP) forecasts, Weather Clim. Dyn., 4, 249–264, https://doi.org/10.5194/wcd-4-249-2023, 2023.

Paschou, P., Siomos, N., Tsekeri, A., Louridas, A., Georgoussis, G., Freudenthaler, V., Binietoglou, I., Tsaknakis, G., Tavernarakis, A., Evangelatos, C., von Bismarck, J., Kanitz, T., Meleti, C., Marinou, E., and Amiridis, V.: The eVe reference

750 polarisation lidar system for the calibration and validation of the Aeolus L2A product, Atmos. Meas. Tech., 15, 2299–2323, https://doi.org/10.5194/amt-15-2299-2022, 2022.

Paschou, P., Siomos, N., Marinou, E., Idrissa, S. M., Quaye, D. T., Attannon, D. D. F., Meleti, C., Bismarck, J. von, Fehr, T., and Amiridis, V.: eVe Lidar Measurements during the ASKOS/JATAC Campaign, Environ. Sci. Proc. 2023, Vol. 26, Page 168, 26, 168, https://doi.org/10.3390/ENVIRONSCIPROC2023026168, 2023.

755 Rani, S. I., Jangid, B. P., Kumar, S., Bushair, M. T., Sharma, P., George, J. P., George, G., and Das Gupta, M.: Assessing the quality of novel Aeolus winds for NWP applications at NCMRWF, Q. J. R. Meteorol. Soc., 148, 1344–1367, https://doi.org/10.1002/QJ.4264, 2022.

Ratynski, M., Khaykin, S., Hauchecorne, A., Wing, R., Cammas, J.-P., Hello, Y., and Keckhut, P.: Validation of Aeolus wind

profiles using ground-based lidar and radiosonde observations at Réunion island and the Observatoire de Haute-Provence,
760   Atmos. Meas. Tech., 16, 997–1016, https://doi.org/10.5194/amt-16-997-2023, 2023.

Reitebuch, O.: The Spaceborne Wind Lidar Mission ADM-Aeolus, edited by: Schumann, U., Springer Berlin Heidelberg,
Berlin, Heidelberg, 815–827, https://doi.org/10.1007/978-3-642-30183-4_49, 2012.

Reitebuch, O., Lemmerz, C., Lux, O., Marksteiner, U., Rahm, S., Weiler, F., Witschas, B., Meringer, M., Schmidt, K., Huber,
D., Nikolaus, I., Geiss, A., Vaughan, M., Dabas, A., Flament, T., Stieglitz, H., Isaksen, L., Rennie, M., de Kloe, J., Marseille,
765   G.-J., Stoffelen, A., Wernham, D., Kanitz, T., Straume, A.-G., Fehr, T., von Bismarck, J., Floberghagen, R., and Parrinello,
T.: Initial Assessment of the Performance of the First Wind Lidar in Space on Aeolus, EPJ Web Conf., 237, 01010,
https://doi.org/10.1051/epjconf/202023701010, 2020.

Rennie, M., Tan, D., Andersson, E., Poli, P., Dabas, A., De Kloe, J., Marseille, G.-J., and Stoffelen, A.: Aeolus Level-2B
algorithm theoretical basis document (mathematical description of the Aeolus Level-2B processor), 12–23 pp., 2020.

770   Rennie, M. P., Isaksen, L., Weiler, F., de Kloe, J., Kanitz, T., and Reitebuch, O.: The impact of Aeolus wind retrievals on
ECMWF global weather forecasts, Q. J. R. Meteorol. Soc., 147, https://doi.org/10.1002/qj.4142, 2021.

Shipley, S. T., Tracy, D. H., Eloranta, E. W., Trauger, J. T., Sroga, J. T., Roesler, F. L., and Weinman, J. A.: High spectral
resolution lidar to measure optical scattering properties of atmospheric aerosols 1: Theory and instrumentation, Appl. Opt., 22,
3716, https://doi.org/10.1364/AO.22.003716, 1983.

775   Tan, D. G. H., Andersson, E., Fisher, M., and Isaksen, L.: Observing-system impact assessment using a data assimilation
ensemble technique: Application to the ADM - Aeolus wind profiling mission, Q. J. R. Meteorol. Soc., 133,
https://doi.org/10.1002/qj.43, 2007.

Tan, D. G. H., Andersson, E., Kloe, J. De, Marseille, G.-J., Stoffelen, A., Poli, P., Denneulin, M.-L., Dabas, A., Huber, D.,
Reitebuch, O., Flamant, P., Rille, O. Le, and Nett, H.: The ADM-Aeolus wind retrieval algorithms, Tellus A Dyn. Meteorol.
780   Oceanogr., 60, 191–205, https://doi.org/10.1111/j.1600-0870.2007.00285.x, 2008.

Walther, B. A. and Moore, J. L.: The concepts of bias, precision and accuracy, and their use in testing the performance of
species richness estimators, with a literature review of estimator performance, Ecography (Cop.)., 28, 815–829,
https://doi.org/10.1111/J.2005.0906-7590.04112.X, 2005.

Wang, P., Donovan, D. P., van Zadelhoff, G.-J., de Kloe, J., Huber, D., and Reissig, K.: Evaluation of Aeolus feature mask
785   and particle extinction coefficient profile products using CALIPSO data, Atmos. Meas. Tech., 17, 5935–5955,
https://doi.org/10.5194/amt-17-5935-2024, 2024.

Wehr, T., Kubota, T., Tzeremes, G., Wallace, K., Nakatsuka, H., Ohno, Y., Koopman, R., Rusli, S., Kikuchi, M., Eisinger, M.,
Tanaka, T., Taga, M., Deghaye, P., Tomita, E., and Bernaerts, D.: The EarthCARE mission - science and system overview,
Atmos. Meas. Tech., 16, 3581–3608, https://doi.org/10.5194/AMT-16-3581-2023, 2023.

790   Weissmann, M. and Cardinali, C.: Impact of airborne Doppler lidar observations on ECMWF forecasts, Q. J. R. Meteorol.
Soc., 133, https://doi.org/10.1002/qj.16, 2007.

Winker, D. M., Pelon, J., Coakley, J. A., Ackerman, S. A., Charlson, R. J., Colarco, P. R., Flamant, P., Fu, Q., Hoff, R. M.,

Kittaka, C., Kubar, T. L., Le Treut, H., McCormick, M. P., Mégie, G., Poole, L., Powell, K., Trepte, K., Vaughan, M. A., and Wielicki, B. A.: The Calipso Mission: A Global 3D View of Aerosols and Clouds, Bull. Am. Meteorol. Soc., https://doi.org/10.1175/2010BAMS3009.1, 2010.

795

Witschas, B., Lemmerz, C., Geiß, A., Lux, O., Marksteiner, U., Rahm, S., Reitebuch, O., and Weiler, F.: First validation of Aeolus wind observations by airborne Doppler wind lidar measurements, Atmos. Meas. Tech., 13, 2381–2396, https://doi.org/10.5194/amt-13-2381-2020, 2020.

Witschas, B., Lemmerz, C., Geiß, A., Lux, O., Marksteiner, U., Rahm, S., Reitebuch, O., Schäfler, A., and Weiler, F.: Validation of the Aeolus L2B wind product with airborne wind lidar measurements in the polar North Atlantic region and in the tropics, Atmos. Meas. Tech., 15, 7049–7070, https://doi.org/10.5194/amt-15-7049-2022, 2022.

800

Yorks, J. E., McGill, M. J., Scott, V. S., Wake, S. W., Kupchock, A., Hlavka, D. L., Hart, W. D., and Selmer, P. A.: The Airborne Cloud–Aerosol Transport System: Overview and Description of the Instrument and Retrieval Algorithms, J. Atmos. Ocean. Technol., 31, 2482–2497, https://doi.org/10.1175/JTECH-D-14-00044.1, 2014.

805

van Zadelhoff, G.-J., Donovan, D. P., and Wang, P.: Detection of aerosol and cloud features for the EarthCARE atmospheric lidar (ATLID): the ATLID FeatureMask (A-FM) product, Atmos. Meas. Tech., 16, 3631–3651, https://doi.org/10.5194/amt-16-3631-2023, 2023.

Zuo, H., Hasager, C. B., Karagali, I., Stoffelen, A., Marseille, G.-J., and de Kloe, J.: Evaluation of Aeolus L2B wind product with wind profiling radar measurements and numerical weather prediction model equivalents over Australia, Atmos. Meas.

810

Tech., 15, 4107–4124, https://doi.org/10.5194/amt-15-4107-2022, 2022.